

ELECTRODEPOSITION OF CO-MN AND CU-MN BASED SPINELS ONTO SOLID
OXIDE FUEL CELL INTERCONNECTS

ELECTRODEPOSITION OF CO-MN AND CU-MN BASED SPINELS ONTO SOLID
OXIDE FUEL CELL INTERCONNECTS

By

XAVIER DANIEL MICHAUD, B.ENG

A Thesis Submitted to the School of Graduate Studies in Partial Fulfilment of the
Requirements for the Degree Master of Applied Sciences

McMaster University

© Copyright by Xavier Michaud, December 2012

MASTER OF APPLIED SCIENCE (2012)
(Materials Science and Engineering)

McMaster University
Hamilton, Ontario

TITLE: Electrodeposition of Co-Mn and Cu-Mn based Spinels onto Solid Oxide Fuel
Cell Interconnects

AUTHOR: Xavier Daniel Michaud, B.Eng (Dalhousie University)

SUPERVISOR: Professor Anthony Petric

NUMBER OF PAGES: **XIII, 101**

Abstract

Solid oxide fuel cells are an efficient method of converting hydrocarbon fuels to electrical power. However, due to some problems with poisoning, these have made no headway in the energy market. The evaporation of chromium oxides from metallic current collectors causes rapid degradation of the cells on the cathode side. It has been shown that spinel coatings reduce the effects of chromium oxide evaporation. In this thesis, two spinel systems are explored for potential application. Cobalt-manganese spinel is a stable spinel which have a wide range of composition, while remaining sufficiently conductive. Copper-manganese spinel, which is much more conductive than cobalt-manganese, is slightly less stable, but nonetheless a candidate. All components of the spinels explored can be electrodeposited from aqueous solutions, at room temperature. By controlling the concentrations of metallic ions, and other additives, coatings can be deposited on interconnecting plates with reproducible results. The newly coated interconnects can be oxidized in-situ. For characterization, the samples for this thesis were oxidized at 800°C. Two substrate materials were used, ferritic stainless steel and a chromium-iron alloy. Stainless steel substrates showed good coating adhesion, but high concentrations of iron were found in the spinel structure. Chromium alloy substrates were better protected by spinel coatings. However, nitride formation at the substrate interface caused localized delamination of the coating. It was shown that plating operations can be scaled up to 10 cm by 10 cm plates, with little modification of the processes used.

Acknowledgements

I would like to first thank my supervisor, Dr Anthony Petric, for offering me the opportunity to pursue my dreams. I appreciate his mentorship, support, and dedication to this project and myself. Providing me with constant advice, while allowing me to explore the topic on my own, was a great learning experience. I am eager to continue my education under his banner.

I would also like to thank the members of the Canadian Center Electron Microscopy for their aid and guidance with SEM imaging. Specifically, I would to thank Chris Butcher, and Dr de Silveira for all the technical help and advice. Their support has allowed me to gain proficiency with valuable equipment. I also appreciate the work done by the members of the McMaster Analytical X-Ray Diffraction Facility for their help with characterization of many samples.

Special thanks go to the staff of the Materials Science and Engineering department, without whom, this experience would have been much more confusing. Their endless dedication to the department has provided me with an unforgettable experience.

I would like to thank the members of this research group, past and present. In particular, conversations with Dr Reza Bateni, Dr Simon Joshi, and Dr Ping Wei have given me background information to build on. Their support and troubleshooting throughout this degree allowed me to focus on finding solutions to every problem that I encountered. I would also like to thank Andrew Scullion, for his input early on in the project.

To my family, I extended the greatest gratitude. Without them, I would not be the man I am today. Their support throughout my education has given me the passion that I currently follow. Also, I thank them for reaching deep into their pockets at a moment's notice.

Lastly, but most importantly, I must express gratitude that no word can describe to my fiancé Chiao-Ting Shen. Her endless sacrifices in the past two years have given me the will to fight-on through the many hardships we have faced together.

Table of Contents

Abstract	III
Acknowledgements	IV
List of Tables.....	IX
List of Figures	X
1. Introduction.....	1
Background & Motivation.....	1
Objectives & Organization of the Thesis	3
2. SOFC Operation and Chromium Poisoning	4
Solid Oxide Fuel Cells.....	4
Chromium Evaporation and Poisoning.....	6
Protective Spinel Coatings.....	8
Cobalt-Manganese System.....	8
Copper-Manganese System.....	10
Additives to Two-Metal Spinel	11
3. Electrodeposition	12
Fundamentals of Electrodeposition	12
Anodes	15
Electrode Potentials and the EMF Series	16

Hydrogen Overpotential.....	18
Hydrogen Evolution.....	18
Plating Bath Composition and Components.....	19
Effects of pH.....	21
Effects of Temperature.....	23
Electrodeposition of Copper.....	23
Effects of impurities.....	24
Displacement Deposition of Copper onto Cobalt.....	25
Electrodeposition of Nickel.....	25
Electrodeposition of Cobalt.....	27
Electrodeposition of Manganese.....	28
Importance of Substrate Cleanliness.....	30
4. Sample Preparation.....	32
Test coupons.....	32
Industrial chromium plates.....	33
Electrodeposition.....	34
Electrodeposition of Copper.....	35
Electrodeposition of Nickel.....	35
Electrodeposition of Cobalt.....	36

Electrodeposition of Manganese.....	36
Solution Replenishment.....	37
Oxidation of Test coupons.....	38
Preparation of Samples for Analysis.....	39
Thermodynamic Models.....	40
5. Results of Electrodeposition.....	41
Nickel Deposition.....	41
Copper Deposition.....	43
Cobalt Deposition.....	44
Manganese Deposition.....	54
Coating Composition Results by ICP.....	61
6. Oxidation of Metallic Coatings.....	63
Cobalt-Manganese (MnCo_2O_4) Spinel Coating.....	64
Cobalt-Manganese ($\text{MnCu}_{\text{Disp}}\text{Co}_{(2-\text{Disp})}\text{O}_4$) Spinel Coating with Thin Copper Interlayer	68
Cobalt-Copper-Manganese ($\text{MnCu}_{(0.5+\text{Disp})}\text{Co}_{(1.5-\text{Disp})}\text{O}_4$) Spinel Coating.....	69
Nickel concentrated Copper-Manganese ($\text{Ni}_{0.5}\text{Cu}_{0.7}\text{Mn}_{1.8}\text{O}_4$) Spinel Coating.....	72
High-Manganese Copper-Nickel ($\text{Ni}_{0.1}\text{Cu}_{0.7}\text{Mn}_{2.2}\text{O}_4$) Spinel Coating.....	73
Copper-Nickel-Manganese ($\text{Ni}_{0.1}\text{Cu}_{1.1}\text{Mn}_{1.8}\text{O}_4$) Spinel Coating.....	76

Semi-Stable Metallic Deposits	78
Coating Damage and Defects	81
Coating at Edges	85
7. Summary and Conclusions	86
Future Work.....	87
8. Bibliography	88
Appendix A: Low Magnification Cross-sections Images	92
Appendix B: Material Analysis.....	96
Appendix C: Pourbaix Diagram for various aqueous metal ions.....	100

List of Tables

Table 3-1: Electromotive Force Series.....	17
Table 4-1: Composition of substrate, by weight %, materials used in coating oxidation tests.....	32
Table 4-2: Solution replenishment rates based on CE and current densities used.....	37
Table 5-1: Effects of starting pH on Nickel coatings.....	41
Table 5-2: Effects of bath starting pH on cobalt coating cohesion.....	54
Table 5-3: Results of ICP performed on different coatings.....	61
Table 6-1: Investigated spinel samples.....	63

List of Figures

Figure 2-1: Standard state voltages of H ₂ and CH ₄ fuels with respect to temperature.	5
Figure 2-2: Partial pressures of some volatile Cr species [Reconstructed from Factsage].	7
Figure 2-3: Phase diagram for cobalt and manganese in the presence of air.	9
Figure 2-4: Copper-manganese phase diagram in the presence of air.	10
Figure 4-1: Masking pattern for test coupons. The grey area demonstrates the area exposed for coating.	33
Figure 5-1: Defective nickel coating due to pH.	42
Figure 5-2: As plated copper deposit on chromium substrate.	44
Figure 5-3: Unprotected pore from copper deposition.	44
Figure 5-4: Mn plated on 100 cm ² cobalt-coated sample without Cu interlayer.	46
Figure 5-5: Mn plated on 100 cm ² cobalt-coated sample with Cu interlayer.	46
Figure 5-6: Cross-section of a cobalt coating plated from 1.3 M CoCl ₂ + 0.5 M boric acid.	47
Figure 5-7: Top-down view of a cobalt coating plated from 1.3 M CoCl ₂ + 0.5 M boric acid near sample edge.	48
Figure 5-8: Top-down view of a cobalt coating plated from 1.3 M CoCl ₂ + 0.5 M boric acid at sample center.	49
Figure 5-9: Top-down view of a cobalt coating plated from 1.3 M CoCl ₂ + 0.5 M boric acid at transition from edge to center.	50
Figure 5-10: Top-down view of a cobalt coating plated from 1.3 M CoCl ₂ + 0.5 M boric acid at nodular-dendritic transition.	50

Figure 5-11: Top-down view of dendrite occurrence in cobalt deposit after electropolishing step. Plated in 1.3 M CoCl ₂ .	51
Figure 5-12: Top-down view of a cobalt coating plated from 0.32 M CoCl ₂ near sample edge.	52
Figure 5-13: Top-down view of a cobalt coating plated from 0.32 M CoCl ₂ at sample center.	53
Figure 5-14: Smooth metallic cobalt coating obtained from a pH 2.30 solution.	54
Figure 5-15: Damaged, but metallic, cobalt coating obtained from pH 6.23 solution.	54
Figure 5-16: Edge effects at lower hole when Mn was plated at 70 mA·cm ⁻² on cobalt coated chromium.	56
Figure 5-17: Lack of edge effects at lower hole when Mn was plated at 70 mA·cm ⁻² on cobalt coated chromium with additional mask.	56
Figure 5-18: Transition from "burnt" to thick manganese coating.	58
Figure 5-19: Continuous manganese found at the center of a deposit.	59
Figure 5-20: Manganese deposited on Cu with NH ₂ OH·HCl.	60
Figure 5-21: Manganese deposited on Co with NH ₂ OH·HCl.	60
Figure 6-1: MnCo ₂ O ₄ on stainless Steel after 120 hours (ID 114-1b).	65
Figure 6-2: MnCo ₂ O ₄ on Cr-5Fe substrate oxidized for 24 hours (ID 124-3).	66
Figure 6-3: MnCo ₂ O ₄ on Cr-5Fe substrate oxidized for 120 hours (ID 114-1a).	68
Figure 6-4: MnCo _(1.5-Disp) Cu _(0.5+Disp) O ₄ on 430 SS substrate oxidized for 120 hours (ID 114-3b). The box and arrow highlight a chromium-rich spinel formed in the coating.	69

Figure 6-5: $\text{MnCo}_{(1.5\text{-Disp})}\text{Cu}_{(0.5\text{+Disp})}\text{O}_4$ on Cr-5Fe substrate oxidized for 24 hours (ID 124-4a).....	70
Figure 6-6: $\text{MnCo}_{(1.5\text{-Disp})}\text{Cu}_{(0.5\text{+Disp})}\text{O}_4$ on Cr-5Fe substrate oxidized for 120 hours (ID 114-3a). The section highlighted by a box emphasizes dendrite formation in the spinel structure.....	71
Figure 6-7: $\text{Cu}_{0.7}\text{Ni}_{0.5}\text{Mn}_{1.8}\text{O}_4$ spinel coating oxidized for 120 hours on Cr-5Fe (ID 117-1).	72
Figure 6-8: $\text{Ni}_{0.1}\text{Cu}_{0.7}\text{Mn}_{2.2}\text{O}_4$ spinel coating oxidized for 120 hours on 430 SS (ID 121-1). The box highlights the region rich with copper in the coating.....	73
Figure 6-9: $\text{Ni}_{0.1}\text{Cu}_{0.7}\text{Mn}_{2.2}\text{O}_4$ spinel coating oxidized for 24 hours on Cr-5Fe (ID 124-1). Outlined area denotes a copper free manganese spinel phase.....	74
Figure 6-10: $\text{Ni}_{0.1}\text{Cu}_{0.7}\text{Mn}_{2.2}\text{O}_4$ spinel coating oxidized for 120 hours on Cr-5Fe (ID 117-2).....	75
Figure 6-11: $\text{Ni}_{0.1}\text{Cu}_{1.1}\text{Mn}_{1.8}\text{O}_4$ spinel coating oxidized for 120 hours on 430 SS (ID 121-2).....	76
Figure 6-12: $\text{Ni}_{0.1}\text{Cu}_{1.1}\text{Mn}_{1.8}\text{O}_4$ spinel coating oxidized for 24 hours on Cr-5Fe (ID 124-2).	77
Figure 6-13: $\text{Ni}_{0.1}\text{Cu}_{1.1}\text{Mn}_{1.8}\text{O}_4$ spinel coating oxidized for 120 hours on Cr-5Fe (ID 118-2). Boxed highlights a chromium-rich spinel formed. This is a rare occurrence.....	78
Figure 6-14: Start of DIffusion and Oxidation Processes.....	79
Figure 6-15: Intermediate step in diffusion and oxidation.....	80
Figure 6-16: Steady State of diffusion and oxidation process.....	80

Figure 6-17: Inclusion of aluminium (or alumina) on Cr-5Fe substrate surface.	82
Figure 6-18: Silica grain preventing adhesion of coating.	82
Figure 6-19: Large bubbling effect found in a Cu-Mn coating on 430 SS.	83
Figure 6-20: Successive small bubbling in Co-Mn coating on Cr-5Fe.	83
Figure 6-21: Coating failure at spinel-chromia interface.	84
Figure 6-22: Coating failure at chromia-substrate interface.	84
Figure 6-23: Common oxidation product at sample edge.	85

1. Introduction

Background & Motivation

The hydrogen-oxygen fuel cell was first identified by Christian Friedrich Schoenbein in 1839 (Huang & Goodenough, 2009). Shortly after, experimental work of William Grove showed that these cells had potential as power-generating devices. However, it took until the end of the nineteenth century before the concept of solid state transport in the oxygen solid electrolyte was discovered. In 1937, the concept of the SOFC was demonstrated. Crude materials were used in its construction, where zirconia was the electrolyte, with Fe_3O_4 and carbon as electrodes. Ongoing research in the materials has continually improved the stability of the cell, enhancing the fuel efficiency of SOFCs. Processing of SOFC materials have advanced such that thin electrolyte material could be applied to porous anodes, which lead to the development of anode-supported SOFCs. This design, along with decreased working temperatures, allowed for a shift in the material of the interconnect. Expensive ceramic materials were replaced by chromium-rich steel alloys. The reduced cost and increased efficiency of these SOFCs have lead industry to adopt a planar design for manufacturing (Press, Santhanam, Miri, Bailey, & Takacs, 2009).

SOFCs have many advantages as power-generating devices. A large advantage of SOFCs over other kinds of fuel cell types is its ability to reform and use light hydrocarbon gas as fuel. This allows it to compete with more traditional methods of power generation. Since SOFCs convert chemical energy directly into electric power, it is inherently more

efficient than standard heat engines. Additionally, these fuel cells operate at elevated temperatures, up to 1000°C, providing high quality waste heat. The combined recovery of waste heat and energy production allows for energy efficiency as high as 90%. Having few moving parts, the SOFC systems are substantially quieter and produce fewer vibrations than traditional combustion systems. Due to certain issues however, they have made limited commercial headway.

One such issue is the reaction of chromium oxides on the surface of interconnects with dry or humid air which forms gaseous products. These products poison the oxygen reduction reaction at the cathode. The degradation of SOFC performance from this effect is substantial enough to kill the SOFC system. It is reported that several coatings exhibit properties that drastically reduce the degradation of the cells by preventing the production of volatile chromium oxides. Two such coatings use perovskite (Pattarkine, Dasgupta, & Virkar, 2008) or spinel ceramic materials (Batani, Wei, Deng, & Petric, 2007; Shaigan, Qu, Ivey, & Chen, 2010). Although perovskite coatings have more desirable properties than those of spinels, their cost and manufacturing methods can be limiting. It is the goal of this thesis to test the ability of spinels to replace perovskites as functional coatings.

Objectives & Organization of the Thesis

There were three primary objectives for this project:

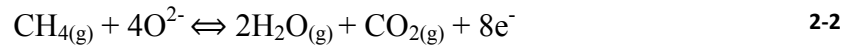
1. To develop an electrodeposition scheme for coating interconnects using aqueous metal-ion solutions.
2. To compare the effects of two common substrate materials on the coatings during oxidation. The substrates used were UNS 430 stainless steel, and a 95% chromium-5% iron alloy.
3. To scale up the electrodeposition process to coat full scale interconnect plates. Industrial plates have an area of 100 cm².

A literature review on SOFC operation, including a more in-depth look at the poisoning effects of chromium, is presented in Chapter 2. Electrodeposition of metallic deposits from aqueous solutions is examined in Chapter 3. The experimental procedures for both production and qualification are described and explained in Chapter 4. Chapters 5 and 6 contain the results of electrodeposition and oxidation of coatings.

2. SOFC Operation and Chromium Poisoning

Solid Oxide Fuel Cells

Solid oxide fuel cells generate electrical power from chemical energy. An oxidant, usually oxygen from air, undergoes a reduction reaction within a porous cathode, as per Equation 2-1. The oxygen ion is transported from the cathode to the anode by way of a dense, ion-conductive electrolyte material. Once at the anode, the fuel is oxidized, producing power. SOFCs commonly use either methane (CH₄) or hydrogen (H₂) as fuels. Equation 2-2 describes the oxidation of CH₄, while Equation 2-3 describes that of H₂.



The electrochemical oxidation of the fuel follows the Nernst equation. The electromotive force (EMF) of the cell is determined by Equation 2-4 for any given oxidation reaction in the form of Equation 2-5.

$$E = E^o + \frac{RT}{zf} \ln \frac{a_C^c a_D^d}{a_A^a a_B^b} \quad 2-4$$



The EMF for reactants and products in their standard state, E^o , is defined by the Gibbs energy change of the reaction. Here, f is Faraday's constant, or 96486 C/mol. The value of E^o can severely decrease with temperature, which can have profound effects on the fuel cell voltage. Figure 2-1 shows the E^o of both H₂ and CH₄ fuels (Huang & Goodenough, 2009). It can be seen that the E^o of H₂ drops greatly with increasing

temperature. However, CH₄ provides a steady E° value throughout the temperature range, making it ideal for energy production in different operating conditions.

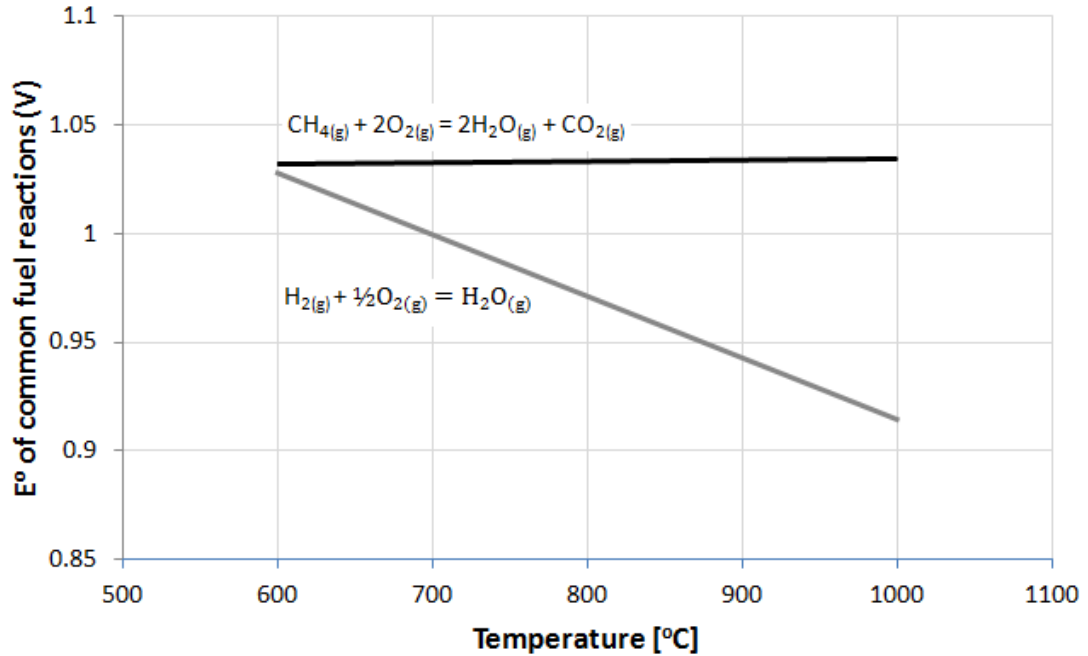


Figure 2-1: Standard state voltages of H₂ and CH₄ fuels with respect to temperature.

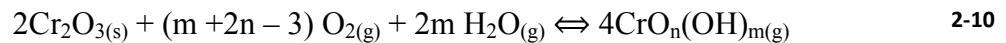
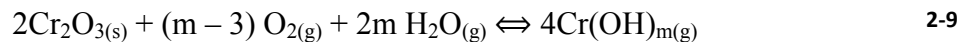
The cell voltage is further shifted by operating conditions other than temperature. The pressure ratios of the oxidant, fuel, and products also limit the potential of the cell. In most cases, air is the choice oxidant, with an oxygen partial pressure of 0.21 atm. Equation 2-6 defines the voltage of the fuel cell using H₂ fuel, while 2-7 is the equivalent expression for CH₄ fuel.

$$E = E^o - \frac{RT}{2f} \ln \frac{P_{H_2O}}{P_{H_2} P_{O_2}^{1/2}} \quad 2-6$$

$$E = E^o - \frac{RT}{8f} \ln \frac{P_{H_2O}^2 P_{CO_2}}{P_{CH_4} P_{O_2}^2} \quad 2-7$$

Chromium Evaporation and Poisoning

The evaporation of chromium oxide from interconnect plates is a detrimental phenomenon which causes failure in the cathode of planar SOFCs. Most SOFC stacks now use high-chromium content steels as the interconnect material. These specialty alloys were designed to withstand the aggressive environment within the SOFC, while remaining structurally reliable and sufficiently conductive. They form a protective layer of chromium (III) oxide. Chromia is preferred over other passive layers, like silicon and aluminum oxides, because of its relatively high conductivity at SOFC working temperatures (Shaigan, Qu, Ivey, & Chen, 2010). Unfortunately, chromia forms volatile chromium compounds in the presence of oxygen and humidity, especially at high temperatures. There are many different forms of chromium volatiles, most of which fall within oxide, hydroxide, and oxyhydroxide groups. The generic reactions for oxide, hydroxide and oxyhydroxides are given in Equations 2-8, 2-9, and 2-10, respectively (Ebbinghaus, 1993; Hilpert, Das, Miller, Peck, & Weib, 1996).



Of all the volatile species, $CrO_{3(g)}$, $Cr(OH)_{4(g)}$, $CrO_2(OH)_2$, and $CrO_2(OH)_{(g)}$ are the most abundant. Figure 2-2 shows the partial pressures of these species at oxygen and steam partial pressures of 0.21 and 0.02 atm, respectively. It should be noted that the anode side

of the SOFC has negligible levels of volatile chromium, even with high partial pressures of steam. This is due to the fact that the fuel stream has low oxygen partial pressure, limiting the above reactions (Huang & Goodenough, 2009).

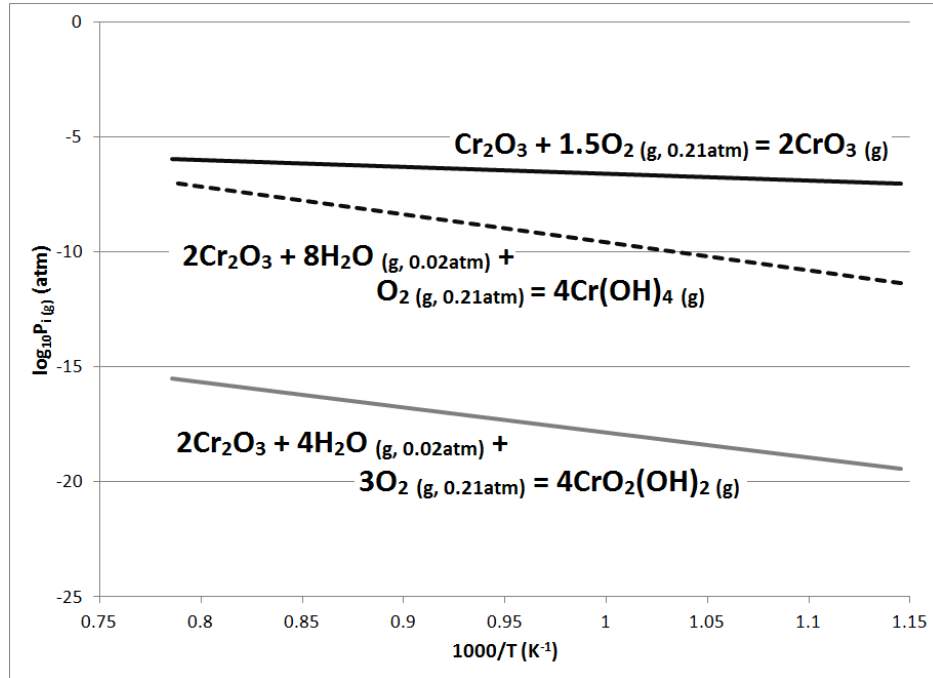


Figure 2-2: Partial pressures of some volatile Cr species [Reconstructed from Factsage].

Newly generated volatile chromium species are transported towards the interface of the cathode and electrolyte. Cathodic reactions reduce the chromium species to the Cr_2O_3 phase. This phase deposits at the reactive sites of the cathode rendering them unusable. These reactions occur rapidly, as does the degradation of cell performance.

The evaporation of chromium can be sufficiently reduced by use of electronically-conductive ceramic coatings. These coatings provide a barrier between the chromium containing interconnect and the cathode atmosphere (Trebbels, Markus, & Singheiser, 2009). Very thin coatings, less than 20 microns, are adequate to prevent cell degradation.

Protective Spinel Coatings

The spinel structure is a cubic closed-packed oxide, with the general formula of $A^{2+}B_2^{3+}O_4$. The A and B cations fill the octahedral and tetrahedral sites in the lattice. Within the normal spinel structure, the A cations occupy the tetrahedral sites, while the B cations occupy the octahedral sites. Variations in the spinel structure can occur, where some B cations are found in tetrahedral sites and A in octahedral. Although the spinel is commonly formed of divalent and trivalent ions, quadrivalent ions can also be present. In some cases, the A and B ions can be the same element with two different charges, as in the manganese spinel Mn_3O_4 , which has an ionic distribution of $Mn^{2+}Mn_2^{3+}O_4$. Although spinels are written in the form of a stoichiometric compound, it is actually a solid solution of multiple oxide phases. This solid solution can have a wide range of composition.

There are several interesting spinel compositions available. Previous work has identified two spinel systems with potential for this application. These were chosen for their high conductivities, but also for the ability to retain chromium. The conductivities of $MnCo_2O_4$ and $Cu_{1+x}Mn_{2-x}O_4$ have been measured as high as 60 and 200 $S \cdot cm^{-1}$, respectively (Petric & Ling, 2007).

Cobalt-Manganese System

The cobalt-manganese spinel is the primary focus of this thesis. This is largely due to the combination of conductivity and stability of spinels containing these elements. Figure 2-3 shows the range of temperature and composition for which the cubic spinel phase is

stable. This ensures that the crystal structure will not change if operating temperatures shifts.

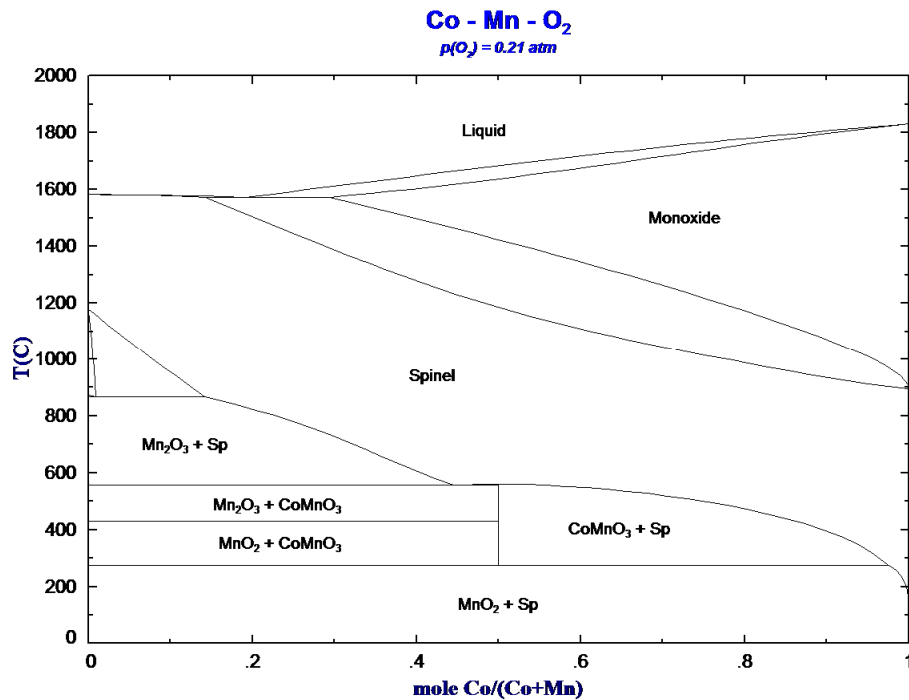


Figure 2-3: Phase diagram for cobalt and manganese in the presence of air.

It has been shown that the conductivity of the spinel will drop very little as the composition varies slightly by either increasing or decreasing manganese content. This means that the coating is not only tolerant to working temperatures, but also to minor composition gradients (Bordeneuve, Tenailleau, Guillemet-Fritsch, Smith, Suard, & Rousset, 2010). However, it has been shown that excessive composition changes will decrease the conductivity. For example, the CoMn₂O₄ and Co₃O₄ spinels have conductivities near 6 S·cm⁻¹, which is one order of magnitude lower than the desired MnCo₂O₄ composition (Petric & Ling, 2007).

Copper-Manganese System

The copper-manganese system is another spinel structure explored in this thesis. Although copper manganese spinel has some instability issues, its high conductivity and inexpensive base elements make it an ideal candidate. Unlike the cobalt-based spinel, the copper-manganese system has a limited temperature and composition range, as seen in Figure 2-4. Additionally, copper has a higher vapour pressure than cobalt and manganese that could potentially cause issues at the cathode side of a cell (Stanislawski, et al., 2007). This means that copper based spinels are likely to be less robust than their cobalt counterparts.

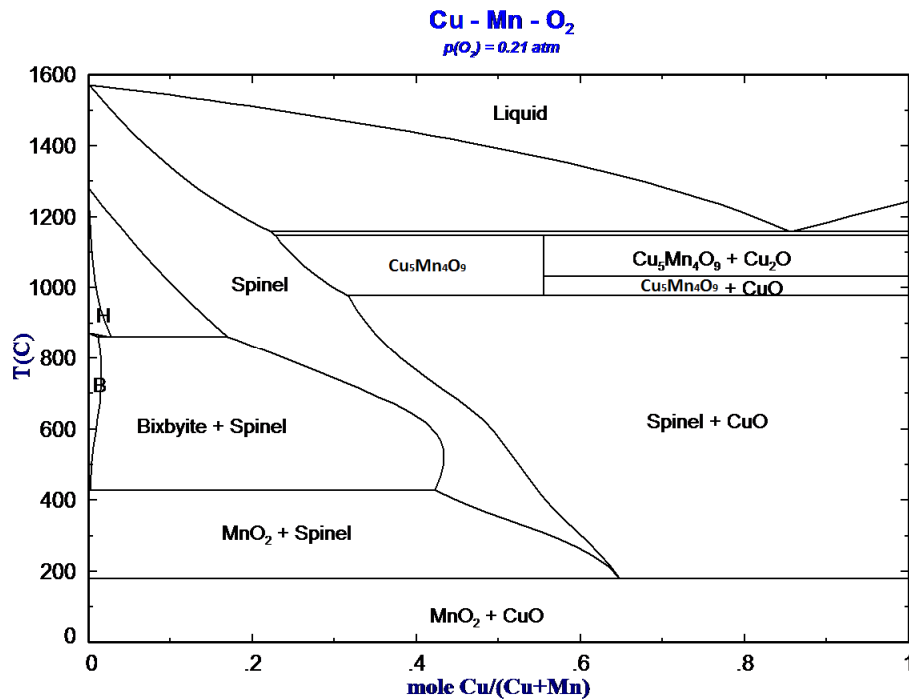


Figure 2-4: Copper-manganese phase diagram in the presence of air.

Additives to Two-Metal Spinel

Slight additions of different metals are explored in both cobalt- and copper-manganese spinels. In the case of copper, the purpose of additions is threefold;

- 1) To provide a better adhesion of copper deposits to the substrate.
- 2) To stabilize the copper-manganese phase, lowering the diffusion of unwanted elements and reducing the vaporization of copper.
- 3) To force the coating to adopt a more favourable structure, increasing the conductivity.

The element of choice for doping copper spinel is nickel. Nickel is inexpensive, easy to deposit, can form a spinel with manganese under the right conditions. It has been seen that nickel is beneficial in copper-spinel, increasing the total conductivity (Baliga & Jain, 1990; Kshirsagar, 1969; Elbadraoui, Baudour, Bouree, Gillot, Fritsch, & Rousset, 1997). On the other hand, Cobalt-manganese spinel does not suffer from the volatility issues of copper-manganese spinel, and does not require additives. However, the possibility of increased electrical-conductivity in cobalt-based spinel is being explored by the addition of copper (Suzuki, 1980; Xu, Wen, Wang, & Wen, 2011; Legros, Metz, & Rousset, 1995). The stability of this copper-doped cobalt-manganese spinel is examined.

3. Electrodeposition

There are multiple methods to apply protective coatings to surfaces. Electrodeposition is chosen for multiple reasons. Simple aqueous solutions are used to electroplate all the required elements found within the spinel coatings investigated. Electrodeposition techniques also can easily be scaled to industrial settings from a laboratory design. This chapter examines the cathodic deposition of metals from aqueous solutions. These metal coatings are then oxidized to form spinel.

Fundamentals of Electrodeposition

Electrodeposition, in the simplest form, uses an electrical current to cause the movement of ions within an electrolyte. Electrolytes must be sufficiently conductive for the process to work. Conductivity in a solution occurs differently than in metals. In metals, a current is caused by the movement of electrons across a potential. This is electronic conduction. In solutions however, the movement of charged matter enables the current to flow. This is called electrolytic conduction (Bard & Faulkner, 2001). When electrical conduction changes from one type to another, a chemical reaction must occur at the electrolyte-electrode interface. Equation 3-1 shows the reduction reactions that occur at the cathode. Positively charged ions transported toward the cathode are reduced from their ionic state by free electrons provided by the electrical current. Negatively charged ions travel towards the anode to be oxidized (Lowenheim, 1978). This can lead to anodic deposition, Equation 3-2, or the evolution of gases, Equation 3-3. In some cases, the anode itself may become a source of electrons, as it is oxidized and dissolved into the solution, described

by Equation 3-4. In cathodic deposition, the effects of the reactions at the anode can sometimes be disregarded.



For a solution to become electrolytically conductive, solutes must at least partially ionize within the solvent. Solutions using acids, bases, and salts are electrolytic conductors.

Faraday's laws of electrolysis are crucial to the electrolytic process. These govern the predictability of electrodeposition. The laws are, as stated by Lowenheim (1978):

“1. The amount of chemical change produced by an electric current is proportional to the quantity of electricity that passes.

2. The amounts of different substances liberated by a given quantity of electricity are proportional to the chemical equivalent weights.”

This means that the mass of material extracted at the cathode from a solution by passing a current is related to both the molecular weight of the ion, and the total charge applied. This is best described by Equation 3-5. Although this equation holds true for the sum of all cell reactions at the cathode, the reaction of interest is seldom the only ongoing reaction. Many side reactions, like the decomposition of water, can occur. This lowers the efficiency of the cell, as it is wasted work. Therefore, Equation 3-5 must be modified by an efficiency factor, or Equation 3-6. The final form, Equation 3-7, can be used to accurately calculate the amount of desired material deposited (Bard & Faulkner, 2001).

$$m = \frac{I \cdot t \cdot MW}{z \cdot f} \quad 3-5$$

$$CE(\%) = 100\% \cdot \frac{m_{dep,Actual}}{m_{dep,Theoretical}} \quad 3-6$$

$$m_{dep} = CE(\%) \frac{I \cdot t \cdot MW_{dep}}{z \cdot f} \quad 3-7$$

In these equations, m and m_{dep} , represent the mass liberated from the process and the mass target material deposited, respectively. The mass is measured in grams. The total current, I , is measured in amperes. The molar weight of the target element is denoted by MW_{dep} . The time of deposition, t , is measured in seconds.

In electroplating, the thickness of the deposit is generally the important factor, not total mass. As such, the average thickness is proportional to both the deposit mass (or total charge imparted), and the area over which the deposit is distributed. The variable, *current density*, multiplied by the area plated, can be used instead of the total current, I , in Equation 3-5. The notion of current density is indeed important for electroplating. Many coating characteristics depend upon it. These include the character, distribution and growth mechanism of the deposit, and the aforementioned current efficiency. In some cases, the current density can even determine whether a deposit will form. In many cases, the area of the cathode can be difficult to determine due to surface roughness or geometrical complexities (Schlesinger & Paunovic, 2000).

The distribution of the coating thickness across a surface will vary based on the geometry. As such, it can be quite difficult to plate a uniform thickness. Localized current density will increase around the edges or at any protrusion above the surface. On the other hand,

crevices will receive lower current densities. Increasing the distance between anode and cathode can sometimes increase uniformity. However, this has a limited effect beyond a certain separation distance.

Anodes

The anode serves two purposes in the plating design. First, it is required for the completion of the electric circuit. It completes the circuit by removing the electrons supplied by the cathode. The other purpose, which is not always necessary, is to supply metal ions for bath replenishment by dissolution. Anodes that provide metal replenishment are known as active anodes, while those that do not, are known as inert anodes. Both types have their own advantages and disadvantages (Lowenheim, 1978).

Active anodes, which are slowly spent, require more maintenance. Not only do these anodes require replacement after excessive dissolution, they can provide sources of impurities and insoluble matter. A sufficient amount of anodes must be kept in stock to prevent extended operation interruption. Additionally, the anode must be continuously monitored to prevent the formation of passive films. These films, although sufficiently conductive, will negate the advantage of using an active anode (Lowenheim, 1978). The primary advantage of the active anode is that they replenish the solution from a metal source, which is generally cheaper than chemical additions. It is important to note that some anodes will dissolve into the plating solution without the application of a current. This must be taken into account for proper cell operation.

Inert anodes, on the other hand, can be installed permanently. They rarely degrade, change shape or size, and generally are never a source of impurities. However, these anodes can be expensive on their own, and fail to replenish the solution. This means that the bath must be replenished with chemical additions. These additions need to be added on a regular basis to prevent excessive depletion (Lowenheim, 1978). Not only are chemical additives more expensive than equivalent pure metals, they also can cause a shift in anion concentrations. Unless carefully prepared, these additives can also add impurities to the system.

Electrode Potentials and the EMF Series

Metals placed in a solution of their own ions will establish an equilibrium between the tendency for dissolution and deposition. Equation 3-1 is the deposition reaction that occurs without an external current, while the reverse is described by 3-4. Prior to equilibrium, the metal will gain a charge relative to the solution. When dissolution is favoured, the metal will be negatively charged, in contrast to a positive charge when deposition is favoured. The potential between a metal and its solution is called the electrode potential.

One such reaction is used as the base line to measure all other reactions. This is the hydrogen electrode, where hydrogen is bubbled over a platinum electrode in a solution of hydrogen ions. The electrode potential is dependent on the equilibrium reaction of Equation 3-8.



3-8

This phenomenon is strongly related to thermodynamics, and the potential can be defined by Nernst equation, Equation 3-9. In the case where the activity of the ion is unity, the potential is known as the standard electrode potential.

$$E = E^o + \frac{RT}{zf} \ln a_{ion} \quad 3-9$$

Since single electrode potentials cannot be measured individually, they are generally referred to the 0 V of the hydrogen-platinum half reaction. Since the hydrogen-platinum electrodes are difficult to use in practice, other calibrated reference electrodes are used for direct measurements. The electromotive force series, abbreviated in Table 3-1, shows the half-cell potential of selected metals (Lowenheim, 1978). More noble metals, marked as positive relative to hydrogen, tend to remain solid (inert). The base metals, those that are negative relative to hydrogen, tend to dissolve into solution. The metals included in the table are those encountered in this thesis, and some other common metals for reference. It should be noted that manganese, a major constituent in spinel coatings, is the lowest base metal that can be plated from aqueous solutions.

Table 3-1: Electromotive Force Series

<i>Electrode</i>	<i>E^o, V</i>	<i>Electrode</i>	<i>E^o, V</i>
Au ⇌ Au ⁺	+1.68	Co ⇌ Co ²⁺	-0.28
Cu ⇌ Cu ⁺	+0.52	Fe ⇌ Fe ²⁺	-0.44
Cu ⇌ Cu ²⁺	+0.34	Cr ⇌ Cr ²⁺	-0.56
Pt/H ₂ ⇌ H ⁺	0	Cr ⇌ Cr ³⁺	-0.74
Fe ⇌ Fe ³⁺	-0.04	Zn ⇌ Zn ²⁺	-0.76
Sn ⇌ Sn ²⁺	-0.14	Mn ⇌ Mn ²⁺	-1.18
Ni ⇌ Ni ²⁺	-0.25	Na ⇌ Na ⁺	-2.72

In many real cases however, the activity of the metal in the electrode is not unity, since it is alloyed with other metals. Therefore, the activity of the electrode material can have a role on the potential of the cell, as per Equation 3-10.

$$E = E^o + \frac{RT}{zf} \ln \frac{a_{ion}}{a_{metal}} \quad 3-10$$

There are many other concepts that limit the EMF series. First, the notion of pure liquids with metal ion activities is rarely encountered outside laboratory settings. Additives and non-standard concentrations of ions will shift the reactions. Finally, kinetics plays a major factor in any reaction where the movement of ions is considered.

Hydrogen Overpotential

The effects of hydrogen overpotential allow for many metals to deposit from aqueous solutions. For example, at pH around 5, the potential for hydrogen evolution is near -0.3 V (Newbery, 1916). This makes hydrogen nobler than many metals, meaning that theoretically, only hydrogen should be produced. The large activation polarization of hydrogen can inhibit its evolution, and therefore facilitate metal deposition. This is also dependent on the surface of the cathode, the cathode material, current density, and additives found in the solution (Schlesinger & Paunovic, 2000).

Hydrogen Evolution

Hydrogen evolution is one of two competing reactions that occur at the cathode. The other is deposition of the metal. Other reactions can occur at the cathode, but are either thermodynamically or kinetically unfavorable and can therefore be neglected. Other than

hydrogen evolution, dissociated hydrogen atoms may become absorbed onto, and within, the coating surface (Gabe, 1997). This may cause defects such as porosity or hydrogen embrittlement. Hydrogen bubbles may hang on the surface causing holes in the coating. Hydrogen may even affect the morphology of deposits, as seen in copper (Nikolic, Popov, Pavlovic, & Pavlovic, 2006).

In the deposition of certain metals, adsorbed hydrogen may cause hydride formation. The amount of adsorbed hydrogen generally increases with both current density and solution temperature (Gabe, 1997). Hydrogen can also diffuse within coatings to attack grain boundaries, the coating interface and the substrate itself. Usually, metals plated at high current efficiencies are not prone to these issues since little or no hydrogen is produced. However, lower efficiency metals like manganese, chromium and cobalt may need special treatment. It is important to treat these coatings at mid-range temperatures, near 200°C, for extended periods of time. This allows for the hydrogen within the coating and substrate to be extracted slowly from the sample. It is known hydrogen in steel can take up to 24 hours to evolve, since hydrogen removal occurs at an exponential rate (Gabe, 1997).

Plating Bath Composition and Components

The plating solution is made of at least one solute and a solvent. In all cases within this thesis, the solvent is water. The solutes, which are often acids, bases, and salts, have specific purposes. Each addition may play more than one of the following roles in the process (Schlesinger & Paunovic, 2000):

- 1) they are the source of metal ions deposited,
- 2) they form complexes with metal ions deposited,
- 3) they increase the conductivity of the solution,
- 4) they stabilize the solution,
- 5) they help dissolve the anode for solution replenishment,
- 6) they modify case-specific properties of the bath and/or the deposit.

In some cases, plating simple metal ions is insufficient. Adding complexing agents to the solution allows for the metal coating to be deposited from a complex ion. This method can provide enhanced coating properties.

Although metal salts form ionic solutions, which are conductive, some still act as poor conductors. By adding highly ionizing salts, the conductivity of the solution is increased. This allows the system to operate at lower voltages than otherwise possible, reducing operating costs.

The stability of the solution is an important parameter. As it will be explained, the pH of the solution can have profound effects. As such, it can be useful to add buffers to the solution to stabilize the pH. It can also be useful to add strong acids to increase the concentration of hydrogen ions to levels higher than naturally found in the metal salt solution. Other agents prevent the hydrolysis of metal salts. Some metal salts are susceptible to hydrolysis, where their metal hydroxide form is insoluble. This is essentially an irreversible reaction which depletes the solution of metal ions.

For cases when active anodes are used, the prevention of passive film formation is important. Therefore, for cases where passivation of the anode occurs, the addition of

certain ions breaks this passivity. In cases of inert anodes, these types of additives are not required.

Finally, the last type of additive is that which modifies the bath, coating, or both in a specified method. These are generally additives only useful in certain baths, but are often used to control the quality of the coating. Without certain additives, the coating may be brittle, non-adherent, or non-coherent. Additives can also be used to control the growth mechanism of the metal deposit. These can reduce internal stresses, surface morphology and grain sizes. Some additives are used to reduce the effects of hydrogen evolution at the cathode.

Effects of pH

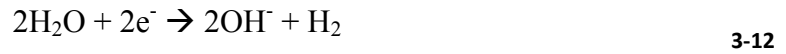
The pH of a plating bath often has some influence on the process. In some cases, as in highly acidic solutions, a slight change in pH is unimportant. This is because the bath's hydrogen ion concentration is elevated, making it difficult to shift the pH in either direction. This is also true in very alkaline baths, where the hydroxide ions are so concentrated that slight variation is insignificant to the process. In the remaining cases, the pH plays an important role in plating operations (Schlesinger & Paunovic, 2000).

The pH will influence many parameters of the plating bath. Unfortunately, most of the effects of pH cannot be easily predicted and must be determined experimentally. Among the more important parameters the pH will affect are the current efficiencies of the cathode and anode. The pH will also affect the adhesion, internal stress and hardness of the deposit. The pH is directly related to the equilibrium of phases within the bath.

During operation, the electrolyte concentration at the anode and cathode can vary locally. The pH at the anode will decrease during operation. For acidic baths, the evolution of oxygen reaction given by Equation 3-11 occurs at the anode (Schlesinger & Paunovic, 2000).



Similarly, at the cathode, the local pH will increase due to the reaction in Equation 3-12. This is the evolution of hydrogen. In cases where the anode and cathode efficiencies are equal, the pH will remain balanced, as the two reactions cancel each other.



However, when the anode has a higher efficiency than the cathode, the bath will become more alkaline. In the reverse case, the solution will become more acidic. When the anode is made of the same material as that being deposited, a balanced bath will operate at constant concentration, since the anode will dissolve. If the pH drops, this indicates that deposition occurs faster at the cathode than dissolution occurs at the anode. The net effect is that the bath is being depleted of metal ions. The opposite case, where the anode dissolves faster, resulting in an accumulation of metal ions in solution. In the case of insoluble anodes, like platinum or graphite, the depletion of metal ions is amplified. The anode does not dissolve forcing metal depletion to occur. Since 3-11 occurs more readily, the pH of the bath will decrease. Additionally, the bath must be replenished by a metal compound. Ideally, the metal compound will also neutralize the excess hydrogen ions.

Effects of Temperature

The temperature of the bath can influence several characteristics of the plating process. While higher temperatures increase the rates of diffusion and ionic mobility (bath conductivity), it does create negative effects. There is an increase in evaporation of the solvent, and hydrolysis occurs more readily (Bard & Faulkner, 2001). Decomposition of some additives can also occur. Like the solution pH, the optimal temperature of a bath must be determined experimentally.

Electrodeposition of Copper

Copper deposition from acid solutions has been used for over 200 years. It is a well explored system, with many different types of baths used for different applications. In this thesis, only copper sulfate solutions are examined.

Solutions made of copper sulfate salts are highly ionized, giving them high conductivity values. Additionally, anode and cathode polarization is small at low current densities. As such, plating of copper occurs at nearly 100% efficiency for convenient current densities. Copper sulfate solutions conventionally used in industry have a concentration between 0.8 and 1.0 mole per liter (Vicenzo & Cavallotti, 2002). These solutions have additions of sulfuric acid (H_2SO_4) of 45 to 90 grams per liter. In unagitated solutions, plating current densities can be as high as $50 \text{ mA}\cdot\text{cm}^{-2}$ without excessive polarization. However if agitation is sufficiently aggressive, acceptable deposits can be extracted at much higher current densities. It should be noted that at extremely high current densities, the deposit will be spongy, and possibly contain entrained salts.

The copper deposit is affected by several parameters. The copper concentration of the solution, as well as the concentration of other additives, including free sulfuric acid, will play a role in the deposition process (Walker & Ward, 1970). At high copper concentrations (1.0 M or more) the resistivity and cathode polarization will both increase slightly. Alternatively, at low concentrations, the cathode current efficiency will decrease. The concentration of free acid in the solution improves the coating characteristics, and some grain refinement can be achieved. Additionally, free acid further reduces the polarization of the electrodes, and prevents the formation of basic salts (eg. $\text{Cu}(\text{OH})_2$). The increase in free acid concentration will decrease the solubility of copper sulfate. Other additives can be added to the sulfate solution, providing a wide range of properties. These are not explored in the scope of thesis.

The temperature of copper plating baths commonly vary between 18° and 60°C. Increases in the working temperature of the bath offer higher conductivities and lower polarization. Lower temperatures, generally below 30°C, provide bright copper films.

Effects of impurities

The anodes of most industrial processes are usually active. These are usually made of cast copper bars or electrolytic copper sheets, which can be sources of impurities. Some impurities commonly found in these anodes are silver, sulfur, lead, tin, nickel, and other base metals. Although copper sulfate solutions are more tolerant of these ionic impurities than most other plating processes, these should be kept low to prevent negative side effects. Although co-deposition of common impurities is difficult, they have been known

to increase polarization of the electrodes, and reduce solution conductivities. Some impurities can co-deposit within the copper coating, causing defects including embrittlement and pitting (Lowenheim, 1978). In an effort to reduce the source of impurities, an inert anode like platinum or graphite can be used.

Displacement Deposition of Copper onto Cobalt

Displacement deposition is a type of electroless deposition. When a substrate of cobalt, or a deposit in our case, is placed in a solution of copper sulfate, cobalt metal forms ions which dissolve into solution. This releases electrons, which reduces copper metal from the solution onto the substrate. This is due to the fact that cobalt is much less noble than copper on the EMF series. Simply stated, two half-cell reactions occur simultaneously at one interface. This type of deposition is self-limiting, and can only produce very thin coatings. The reaction will stop once no more cobalt metal is left exposed to the solution (Schlesinger & Paunovic, 2000).

Electrodeposition of Nickel

Similar to copper, nickel deposition from aqueous solutions has been explored thoroughly. Several baths have been designed for different operations, all of which operate in acidic pH ranges. Much like copper, the nickel industry uses active anodes. To prevent impurity issues, inert anodes were used in laboratory experiments. The plating of nickel occurs at high cathode efficiencies, between 90 and 97 percent. This depends highly on the type of bath, and working parameters. As a rule, the cathode efficiency is stated as 95% for less precise calculations (Schlesinger & Paunovic, 2000).

Nickel deposits are used, in this case, as an interlayer metal, providing a stronger bond between the substrate and the copper deposit. As such, it is important that this layer remains adherent to the substrate. Unfortunately, nickel deposits can have internal stress based on the plating process. The internal stress in deposits is commonly caused by the electro-crystallization process, and when co-deposition of impurities occurs (Lowenheim, 1978). These impurities are commonly hydrogen and sulfur, but others are certainly possible. It is important that these internal stresses be relaxed, or the coating could fail.

The *high-sulfate* bath was chosen for the electrodeposition of nickel, for its simple composition, and its ability to function at lower (room) temperatures. Many other baths operate above 40°C, or produce unnecessary coatings. The *high-sulfate* bath has a nickel sulfate concentration of 0.3 to 0.4 mole per liter. It has additions of sodium sulfate at a concentration of 0.5 to 0.8 mole per liter. Boric acid is added at a concentration of 15 grams per liter. Finally, ammonium chloride is added with a concentration of 0.3 to 0.65 mole per liter. This solution operates within a pH of 5.3 to 5.8, at a current density range of 0.5 mA·cm⁻² to 25 mA·cm⁻² (Schlesinger & Paunovic, 2000). Although these coatings have high reported internal stresses, only thin coatings of less than 1 micron were planned, reducing the risk of stress-caused damage.

Boric acid is added to nickel sulfate solutions for multiple reasons. It has been observed that boric acid buffers the solution pH near the cathode (Tsuru, Nomura, & Foulkes, 2002; Lu, Yang, & Zhang, 2010). Hydrogen evolution is reduced as the concentration of boric acid increases. This has the effect of reducing the internal stresses of the films, but

consequently also increases the cathode current efficiency. This is believed to be due to the increased hydrogen overpotential caused by the formation of nickel borate (Lu, Yang, & Zhang, 2010).

Sodium sulfate is added to the solution to increase the coating adhesion, and increase the solution conductivity. Increases in the current efficiency and a reduction in hydrogen evolution have been reported. This also has been shown in the deposition of cobalt from sulfate salts(Sharma, Alex, Bidaye, & Suri, 2005).

Electrodeposition of Cobalt

Cobalt metal can be deposited from aqueous solutions using various salts. Commonly sulfates and chlorides are used. Although commercial cobalt coatings plated from these solutions are used for unrelated purposes to this thesis, a bath of cobalt chloride at a concentration of around 0.4 mole per liter with additions of 15 grams per liter of boric acid, was satisfactory. This bath operates at temperatures near 50°C, and a pH of 2.5 (Kongstein, Haarberg, & Thonstad, 2007). Studies on the effects of plating parameters on cobalt deposits from chloride solutions are limited. However, it has been seen that the transition from sulfate to chloride solutions is without severe ill effects (Pradhan, Singh, Tripathy, & Das, 2001). As such, the exact parameters of a sulfate bath cannot be transcribed to chloride baths. However, the overall trends of additions, pH and temperature still hold true (Jeffrey, Choo, & Breuer, 2000).

Much like in the deposition of nickel, boric acid is added to buffer the solution pH and reduce the severity of hydrogen evolution. It was shown that boric acid in sulfate

solutions loses its potency at higher plating temperatures (Santos, Matos, Trivinho-Strixino, & Pereira, 2007). However, evidence shows that even with lowered boric acid potency, higher temperatures provide less stressed coatings with higher current efficiencies (Sharma, Alex, Bidaye, & Suri, 2005).

Electrodeposition of Manganese

Manganese deposition is performed using a sulfate solution. Ammonium sulfate is added as an electrolyte for multiple reasons. First, ammonium sulfate increases the conductivity of the solution. It also stabilizes the solution, preventing manganese hydroxides from forming at the cathode during electrodeposition (Wei, Deng, Bateni, & Petric, 2007). By adding ammonium sulfate, the growth of manganese is further aided by an increase in the hydrogen overpotential. This shifts the process to higher current efficiencies, allowing for full coverage to be achieved (Gong & Zangari, *Electrodeposition and Characterization of Manganese Coatings*, 2002).

The pH of the solution is an important parameter for the deposition of manganese. At pH greater than 7, the solution destabilizes, causing rapid precipitation of manganese hydroxides. However, an overly acidic solution will cause the dissolution of manganese from the cathode, and excessive hydrogen evolution. It is shown that the most efficient pH for deposition is higher than 2 and less than 6 (Gong & Zangari, *Electrodeposition and Characterization of Manganese Coatings*, 2002).

The efficiency of the plating process is strongly dependant on the current density applied. When current densities are low, the dissolution of manganese in to solution is strong.

This causes additional hydrogen evolution and a drop in efficiency. If the current density is too low, it is entirely possible that the deposit will not grow, and in cases where it does, the coating is spongy and porous (Gong & Zangari, *Electrodeposition and Characterization of Sacrificial Copper-Manganese Alloy Coatings*, 2004).

There are many additives that increase the current efficiency. Sulfur is commonly added to bulk processes where slight impurities are acceptable, since the amount of sulfur required can be substantial for any considerable improvement (Lewis, Scaife, & Swinkels, 1976). Using selenium dioxide as an additive will provide similar effects as sulfur, but at lower concentrations. Additionally, it has been reported that selenium can increase current efficiencies to nearly 90%, much higher than sulfur additions (Radhakrishnamurthy & Reddy, 1977). However, like sulfur, selenium can be picked up in the coating. These impurities are likely detrimental to spinel formation (Wei, Deng, Bateni, & Petric, 2007). Another additive which is being investigated in the deposition of manganese is hydroxylamine hydrochloride. When coupled with selenium dioxide, it reduces the amount of trapped selenium in the coating (Lewis, Scaife, & Swinkels, 1976). Additional work showed that hydroxylamine could be used to stabilize the solution, preventing and reversing the effects of manganese hydroxide (Sylla, Savall, Gadouleau, Rebere, Creus, & Refait, 2005). This proves useful in preventing or controlling the rate of manganese and other metal hydroxides that form at the anode during electrodeposition.

The manganese deposition process is sensitive to the presence of metal ion impurities. Even low concentrations of copper, iron, nickel, or manganese can reduce the amount of

manganese deposited. If these impurities are present in high concentrations, they can prevent the deposition of manganese completely, by preferentially depositing instead. This phenomenon can actually be controlled, such that manganese coatings can be co-deposited with other elements to form an alloy coating (Gong & Zangari, Increased Metallic Character of Electrodeposited Mn Coatings Using Metal Ion Additives, 2004). However, the concentrations of the impurities must be controlled precisely, which can be difficult in large bath operations. Therefore, these solutions were not explored.

Importance of Substrate Cleanliness

Generally speaking, parts that have been machined, formed, cast or otherwise fabricated will have contaminants on their surfaces. These contaminants must be removed, or electroplated coatings will be non-adherent, incomplete, discoloured, or otherwise unsatisfactory (Lowenheim, 1978). There are many types of contaminants on a surface. The common contaminants are surface oxides and soils. Surface oxides are thin layers of metal oxide which form when the part contacts air, humidity, or another source of oxygen. Soils fall within two categories; organic and inorganic.

Organic soils are generally oils and residues from prior operations. These include animal, mineral, and vegetable oils used for quenching, cooling, and lubrication during work. Another common organic soil is fingerprints. These are commonly removed by alkaline cleaners, or solvents.

Inorganic soils are generally fine solids like dust and dirt, and include tarnish or rust. Many of these will be removed by alkaline cleaners with other organic soils. However,

rust, tarnish, and the surface oxides will remain. In some cases, the alkaline cleaner can cause these types of impurities. To remove these, pickling in acid or electropolishing can be used.

Once suitably clean, the substrate can be placed in the plating bath. It can be difficult, however, to assure surface cleanliness, since most of these contaminants are difficult to detect. The simplest, and most common, method of testing cleanliness is by administering the water-break test. Although this test is not sensitive to minute amounts of contaminants, it is sufficient for most applications. In this test, water is flowed over a cleaned part. If the part is free of organic and hydrophobic soils, the water will flow off the part in an unbroken sheet. Parts with unacceptable levels of contaminants will have areas left unwetted which can be visually detected. Unfortunately, parts that are covered with thin oxide films will still pass this test.

4. Sample Preparation

Coatings were plated onto two types of substrates: ferritic 430 stainless steel and chromium alloy. The composition of the substrate affected the oxidation products. Small test coupons of stainless steel and chromium were used to characterize the coatings. Larger industrial sized plates were used to determine the validity of applying these coatings for customer use. Table 4-1 contains the nominal composition of the 430 stainless steel acquired from McMaster-Carr, and the chromium plates from Stackpole International. Elements which were not reported are marked with a “—” symbol. Stainless steel samples were tested by inductively coupled plasma (ICP) mass spectrometry for a more accurate composition profile. Chromium plates were produced by powder metallurgy methods using high purity metal feeds.

Table 4-1: Composition of substrate, by weight %, materials used in coating oxidation tests.

Material	Fe	Cr	C	Mn	Ni	Cu	P	Co	S
Nominal UNS 430 SS	Bal.	16 – 18	<0.12	<1	—	0	0	—	0
430 SS tested by ICP	Bal.	16.2	0.044	0.29	0.16	0.19	0.32	0.02	0.005
Chromium plates	5	95	—	—	—	—	—	—	—

Test coupons

Test coupons samples were cut from bulk material down to a size of about 2.5x5.0 cm. Stainless steel coupons had a thickness of 1 mm while chromium samples were nearly 5 mm thick. These were then polished using US180 grit SiC paper, followed by a US240 grit SiC paper. The edges of the coupons were also ground to a rounded end. The samples were ultrasonically cleaned using acetone, at 30°C, for at least 1 minute, followed by a rinse using room temperature acetone. The coupons were then masked using consumer

grade masking tape (Grand&Toy 99838/9) such that only an area of 6-7 cm² was exposed to the plating solution. Figure 4-1 shows the masking pattern of typical samples. The rounded edge was formed to reduce the effects of current differentials. Prior to depositing the coating, the test coupons were anodically activated in 10% H₂SO₄ for 1 minute by applying a potential at a current density of 50 mA·cm⁻². The samples were then rinsed and immersed into the first plating solution.

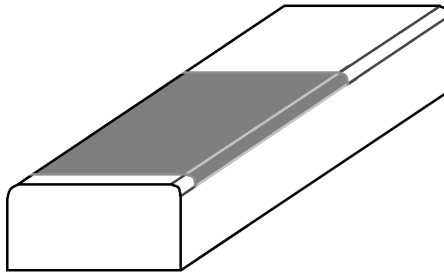


Figure 4-1: Masking pattern for test coupons. The grey area demonstrates the area exposed for coating.

Industrial chromium plates

These flat plates of chromium, provided by Stackpole International, were used to determine if the coatings could be applied on a larger scale. These plates were of 10x10 cm, with little surface detail. One of the two gas ports was used for mounting and electrical contact. Unlike test coupons, the size of the plates made them difficult to grind and polish. The plates were only washed with acetone. The samples were masked such that the edges and back were covered, leaving one flat surface exposed. The mounting holes were also masked to prevent deleterious edge effects. The plates were mounted on a custom-made mounting pin. The whole assembly was cleaned in 10% H₂SO₄ for 1 minute. It was then rinsed and immersed into the cobalt plating solution.

The mounting pin was machined from two copper rods, fitted into an “L” shaped mount. It was then masked with masking tape, and dipped into paint primer to seal any gaps. Two sections of the mounting pin were left unmasked. These were the tips which made contact with the plate and the power source.

Electrodeposition

All samples were plated using cathodic electrodeposition. The counter electrode was platinum. Test coupons were originally plated using computer controlled EG&G 273 potentiostat/galvanostat with a standard calomel reference electrode. Once deposition was standardized, further samples were plated using a two electrode system consisting of a BK Precision 1730 DC power supply and an ammeter with a sensitivity of 1 mA. Samples plated with the two electrode method were reproducible, and of better quality, as bath exchanges could be done in rapid succession. The baths used for test coupon deposition were deep, circular crystallization dishes with an approximate volume of 390 mL, except in the case of manganese deposition, an anode bag was used, contained in a volume of about 1.3 L.

Industrial plates were coated using a two electrode system, since the current required could not be provided by the EG&G potentiostat available. A KEPCO 20-20M bipolar power supply was used to produce currents as high as 20 amperes. The KEPCO power supply was attached to a digital ammeter with a sensitivity of 10 mA. The baths used for these plates were sufficiently large to hold both electrodes. A rectangular bath of 2 L was

used for the deposition of cobalt, while deposition of manganese used a 4 L bath. All solutions used reverse osmosis filtered water as the solvent.

Electrodeposition of Copper

Many methods of depositing metallic copper onto a substrate were available. A 0.8 M copper sulfate bath with a pH near 1.0 was chosen for its simplicity, and consistent application. No other additives were used in the solution except for 40 g·L⁻¹ of H₂SO₄. A current density of 48 mA·cm⁻² was applied to the substrate, giving a coating growth rate of 1 μm per minute. This was calculated with the assumption that copper deposits were fully dense, and had a cathode current efficiency (CE) of 99%. However, electrodeposited copper from a sulfate solution produced uneven coatings on stainless steel and chromium substrates. Plating a thin layer of either cobalt or nickel beforehand allowed for a desirable copper coating to be achieved.

Electrodeposition of Nickel

The primary function of nickel deposits was an interlayer for copper adhesion. As such, a strike deposition method was best. A well used, and safe, method of striking nickel was from a nickel sulfate solution. The solution had a composition of 0.3 M NiSO₄, 0.5 M Na₂SO₄, 0.3 M NH₄Cl, and 0.24 M boric acid. The CE used for this process was the average of 95% for rough calculations, since only thin samples plated for short periods of time were needed. The current density was set at 25 mA·cm⁻², to give a deposit growth

rate of $0.5\mu\text{m}$ per minute. This solution was sensitive to pH changes. Uneven or incomplete coatings would occur if the starting pH was lower than 3.1, or higher than 3.8.

Electrodeposition of Cobalt

The chosen method of plating cobalt was in a 0.33 M cobalt chloride solution with 0.15 M boric acid. This solution allowed plating of a smooth metallic deposit to over a wide pH range at room temperature. A fresh solution had a starting pH of around 2.3, but this value gradually dropped as samples were plated. Cobalt was plated at low current densities, commonly $15\text{ mA}\cdot\text{cm}^{-2}$, to avoid delamination of the deposit at higher rates. The growth rate of cobalt under these conditions was $0.25\mu\text{m}$ per minute. Using mass gain measurements, cobalt deposition had a CE of 75%.

Electrodeposition of Manganese

Manganese can be deposited from sulfate solution without additives (Wei, Hileman Jr, Bateni, Deng, & Petric, 2007). However, hydrogen evolution at the cathode can produce coating defects. Selenium dioxide can reduce hydrogen electrolysis at the cathode sufficiently. A solution of 0.6 M MnSO_4 with 2 mg/L SeO_2 was used with a supporting electrolyte of 1.2 M $(\text{NH}_4)_2\text{SO}_4$. The CE for this solution was 50%, when samples were plated at $100\text{ mA}\cdot\text{cm}^{-2}$. This corresponds to a growth rate of $1.2\mu\text{m}$ per minute. At this current density, the edge effects can be substantial. By reducing the current as low as $40\text{ mA}\cdot\text{cm}^{-2}$, coatings with minimal defects and near-negligible edge effects can be produced. The starting pH of this solution was set to 3.3 ± 0.1 . Hydroxylamine hydrochloride was

added to one solution at a concentration of 2.5 g/L. This had both beneficial and detrimental effects.

Solution Replenishment

The solutions used in the experiments eventually suffer from depletion of electrolytes. As an increasing number of samples are plated using the same solution, the metal ion concentration dropped. This could potentially hinder or alter the plating processes. Therefore, it was determined that solutions would be replenished after every set of samples. Table 4-2 was used to determine the amount of reagent to be added to the solution. These values were calculated using the cathode efficiency of each plating bath, and the current density used in the operation. It can be seen from the table that this depletion can be quite substantial, especially in the case of coating industrial plates. Larger plates will deplete the solution at a faster rate than small coupons. For example, plating a single industrial sized plate with cobalt for 30 minutes will require that the 2.5 g of $\text{CoCl}_2 \cdot 6\text{H}_2\text{O}$ be added to the solution to prevent excessive depletion.

Table 4-2: Solution replenishment rates based on CE and current densities used.

Reagent	Solution Replenishment Rate
$\text{CuSO}_4 \cdot 5\text{H}_2\text{O}$	$0.003726 \text{ g cm}^{-2} \text{ min}^{-1}$
$\text{CoCl}_2 \cdot 6\text{H}_2\text{O}$	$0.000832 \text{ g cm}^{-2} \text{ min}^{-1}$
$\text{NiSO}_4 \cdot 6\text{H}_2\text{O}$	$0.001941 \text{ g cm}^{-2} \text{ min}^{-1}$
$\text{MnSO}_4 \cdot \text{H}_2\text{O}$	$0.002628 \text{ g cm}^{-2} \text{ min}^{-1}$

There were many other additives in the solutions which may or may not deplete. This was especially true for the nickel and manganese bath. In the manganese bath, the other major constituent, $(\text{NH}_4)_2\text{SO}_4$, was assumed to be replenished when the pH was returned to

desired levels using NH_4OH . Similarly, in the nickel bath, NH_4Cl was assumed to be replenished during pH stabilization using NH_4OH . The purity of the reagents used in plating bath solutions can be found in Appendix B.

Oxidation of Test coupons

The newly plated metal coatings were converted to oxide layers in a laboratory box furnace. Within the furnace, a sealed stainless steel container with inlet/outlet tubes was used to hold the samples and contain specified gaseous atmosphere. The gases were passed through DI water at room temperature prior to entering the furnace. Samples were slowly heated to 800°C , where they were held for extended periods of time in flowing air.

It was found that stainless steel samples could be heated, and annealed, in either air or argon as long as the heating rates were slow. Heating rates of 1°C per minute, or less, generated well adherent samples. Increasing the heating rate would cause most samples to delaminate prior to reaching oxidation temperatures. Chromium samples oxidized in air were less susceptible to delamination than their stainless steel counterparts. Samples heated at rates of up to 5°C per minute would show no sign of coating damage. When argon was used in the annealing of chromium samples, the diffusion of chromium into the metallic coating was enhanced, causing the chromia scale to grow thicker than expected. In an attempt to compare the substrate effects on coatings, both types of samples were heated at 1°C per minute in air.

Preparation of Samples for Analysis

Sample analysis was primarily done by scanning electron microscopy (SEM) and x-ray diffraction (XRD) techniques. Prior to processing samples for analysis, they were visually inspected for coating damage and delamination. These defects would occur more readily for samples of stainless steel than those made of chromium. Samples were deemed acceptable for analysis as long as the bulk of the coating was adherent, with only slight coating damage around the edges. Samples destined for XRD analysis were left untouched, and were characterized using a Bruker D8 Advance diffractometer.

Imaging of sample coatings was done by a JEOL JSM-6610 SEM. Surface imaging required that the sample was sufficiently conductive to prevent charging within the chamber. Cross-sections of samples were not only characterized by imaging, but also by energy-dispersive X-ray spectroscopy (EDS) to determine the elemental profiles of the coatings. To obtain the best possible results from EDS, samples were polished to remove all of the surface roughness. They were progressively ground and polished until the surface roughness was smoothed with a colloidal silica suspension. The samples were coated with a thin carbon layer to provide conductivity in the SEM, without adversely interfering with the signals needed for EDS characterization. EDS was performed with an Oxford Instruments X-Max attachment to the JEOL JSM-6610.

Some coatings were removed from the substrate prior to oxidation. These were then tested by ICP for elemental content. This was used to confirm the weight percent, and therefore the thickness, of each element within the coating.

Thermodynamic Models

The FactSage version 6.3 software was used to match certain phases found in the coatings.

The spinel solution phase diagrams were based on in-house modelling. Other phases were available in the standard software package.

5. Results of Electrodeposition

This chapter deals with the results of electrodeposition. Not only were the proper parameters for individual metals important, but each subsequent coating was reliant on the previous. The plating process of each layer had an impact on the final coating properties, whether it was a success or failure.

Nickel Deposition

Nickel sulfate was used to deposit thin nickel deposits onto both types of substrates. In either case, the pH of the solution used was fundamentally different than that reported in books and journals. The literature showed that *high-sulfate* baths required a pH of 5.3 to 5.8. Continuous failures of plated samples led to an investigation into the solution pH, since a new bath had failed to fix the problem. Table 5-1 shows the results of this investigation. Coatings during this investigation were inspected visually, and tested for adhesion. All coatings, whether coherent and uniform or not, passed adhesion tests.

Table 5-1: Effects of starting pH on Nickel coatings.

<i>Starting pH</i>	<i>Ending pH</i>	<i>Coating Quality</i>
2.70	2.49	Non-coherent
3.10	2.70	Non-coherent
3.10	3.00	Non-uniform
3.12	3.09	Coherent, Uniform
3.56	3.45	Coherent, Uniform
3.93	3.78	Coherent, Uniform
4.34	4.17	Coherent, Uniform
5.53	5.48	Non-coherent

Once plated, the nickel coating was strongly bonded and needed to be ground off. However, when pH dropped below 3.1, the coating was uneven, with thicker edges and a thinner center. When the pH dropped below 3.0 during plating, the sample would have

un-plated areas. If the pH was increased to the pH range recommended in literature, the coating would again appear damaged and uneven. Figure 5-1 shows an example of a non-coherent coating, where defects can be seen on the right side of the coating. At the top right corner of the sample, the coating did not plate, leaving exposed stainless steel. The rest of the right side is covered with intermittent nickel.

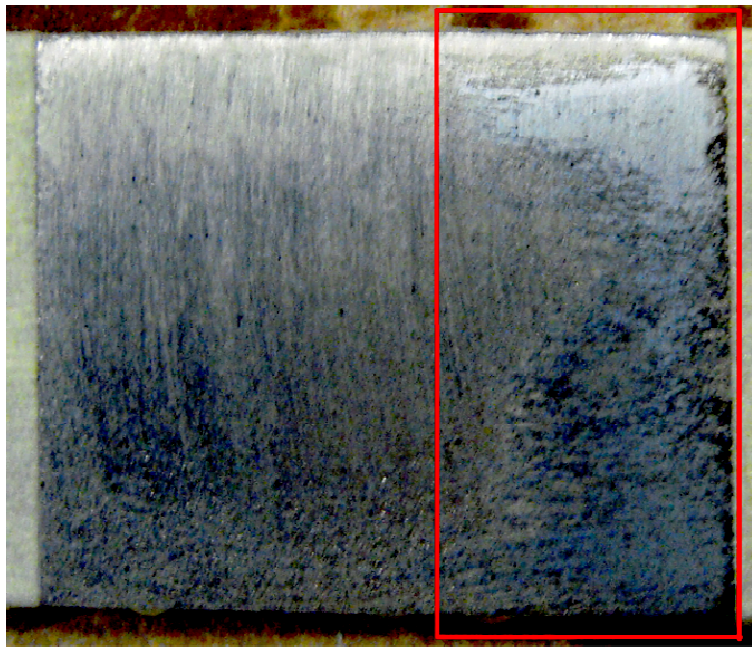


Figure 5-1: Defective nickel coating due to pH.

The current density used for all experiments was $25 \text{ mA}\cdot\text{cm}^{-2}$, with a bath temperature between 18° and 21°C . As a precaution, all subsequent samples were plated at a starting pH between 3.2 and 3.4. This prevented the pH from dropping below the 3.1 threshold.

Nickel metal interlayers later had an associated problem. When spinels of high nickel content were examined, the nickel coating failed to adhere to stainless steel samples.

Samples plated for less than 2 minutes with nickel, an equivalent thickness of 1 micron, adhered well at all times to both substrates. Samples plated for more than 3 minutes failed to adhere to stainless steel, but succeeded on chromium samples. It is believed that the internal stresses found in the nickel coatings were the cause of delamination. This did not occur with the chromium substrate, which could be due to the substrate surface morphology. These samples were fabricated using powder metallurgy, and therefore had more surface roughness due to pores. This may have relieved some of the stress within the nickel coatings.

Copper Deposition

Although copper deposition was the simplest process in this thesis, some issues were quickly identified. The copper deposition process would create low-adhesion, non-continuous films on both chromium and stainless steel substrates. This film had limited success in the deposition of subsequent manganese coatings. Whenever these samples were oxidized, they would bulge, and often delaminate. Figure 5-2 shows the copper coating on chromium, prior to oxidation. Rather than obtaining smooth coatings, small semi-spherical nodules would form, which could be detached with little mechanical work. These were coated at $48 \text{ mA}\cdot\text{cm}^{-2}$ for 4 minutes.

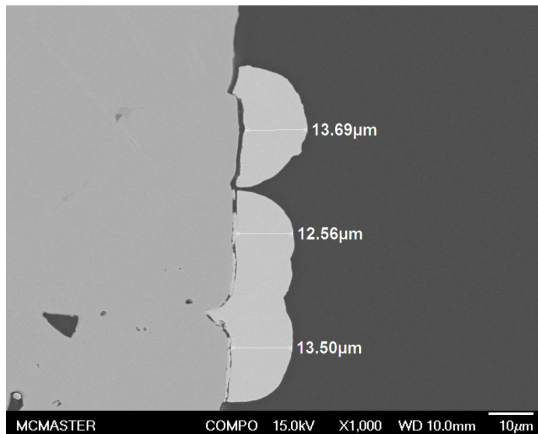


Figure 5-2: As plated copper deposit on chromium substrate.

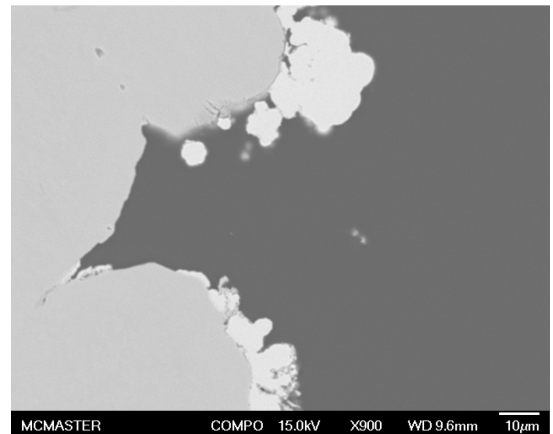


Figure 5-3: Unprotected pore from copper deposition.

Coatings directly applied to chromium or stainless steel substrates also had very little tolerance for surface roughness. Unlike nickel and cobalt, copper did not deposit inside or over pores. These small pores have high internal surface areas which are left unprotected. An example of this open pore is found in Figure 5-3. These unprotected pores are a cause for concern, since a non-continuous coating will still allow for volatile chromium oxides to reach the cathode sites. Therefore, from these two examples, it was determined that copper would be better plated after a thin interlayer was first deposited.

Cobalt Deposition

The original solution used in this work for cobalt deposition was 1.3 M cobalt chloride, and 0.5 M boric acid. This yielded strongly adherent coatings on both chromium and stainless steel substrates. The solution could be used at room temperature, even though optimal current efficiency was near 50°C. Preliminary work with cobalt-manganese spinel required that manganese be plated second, on top of cobalt. Although this was

successful for samples of less than 3 cm², the success rate dropped to less than 50% for plates of 6-7 cm² and to near zero for industrial sized plates.

The original hypothesis for this failure implicated the plating process of manganese, as it was observed on both bare stainless steel and chromium. The edges of the plates formed a thin deposit, while the rest of the substrate would remain bare. After experimentation with the plating parameters for manganese, including anode size, solution composition, and current densities, the problem was determined to be surface related. In one trial, a cathode with a cobalt base coating was dipped in copper sulfate for displacement deposition. This resulted in manganese coating plating at a nearly 100% success rate. This was the case regardless of the size the plate. This indicated that the probable cause of the manganese failure was the underlayer.

Figure 5-4 shows four different sections on the plate. The first, and most obvious, is the rectangular silver area which is labelled “112-2.” This area was uncoated chromium substrate which was masked for design purposes. The center of the plate, “A”, which made up the majority of the surface, exhibited cobalt coating which did not deposit any significant amount of manganese. Around the edges was a thin glossy band of “burnt” manganese coating. It was brittle and easy to remove by simply wiping the surface. The last section, “B”, which was the darkest, was the area between the burnt manganese and the bare cobalt. This was the desired manganese coating. The reason why it was so dark is due to the fact that manganese oxidizes quickly in air.

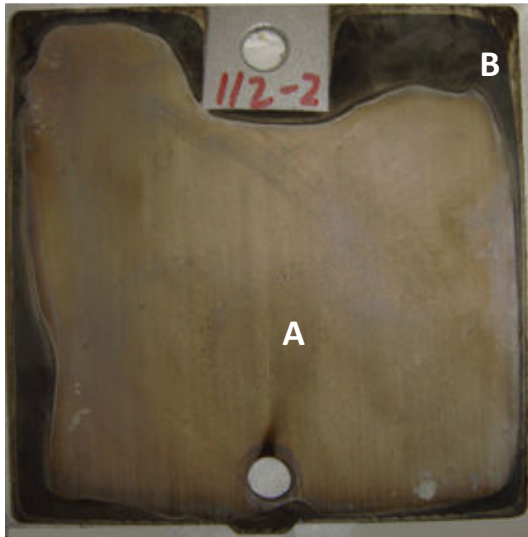


Figure 5-4: Mn plated on 100 cm² cobalt-coated sample without Cu interlayer.



Figure 5-5: Mn plated on 100 cm² cobalt-coated sample with Cu interlayer.

In Figure 5-5, copper was plated on top of cobalt. The manganese then plated successfully. Again, the burnt edge of manganese can be seen. It was of similar size to the one found in Figure 5-4 because the same current density was applied to both plates. However, the entire plate was now covered with manganese. There was no exposed cobalt left. The black defect extending from the left edge to the bottom hole of the plate was due to plating solution dribbling across the surface, after the plate had dried, when the mask was being removed. The blackening occurs due to the dissolution of manganese. This phenomenon can be used to destructively test the presence of manganese, since cobalt does not react violently to acidic liquids while manganese does.

At that time, the effects of copper additions in cobalt-manganese spinels were not being explored. Therefore, having a metallic copper interlayer was unwanted. The surface of the cobalt deposit had to be investigated. Figure 5-6 was taken from a cobalt deposit plated on chromium for 30 minutes at a current density of $15 \text{ mA}\cdot\text{cm}^{-2}$. The most notable feature was the excessive dendrite formation at the free surface. These dendrites would cause localized peaks in current density. This could allow the plating of manganese in certain sections, but would effectively prevent the rest of the plate from receiving a coating.

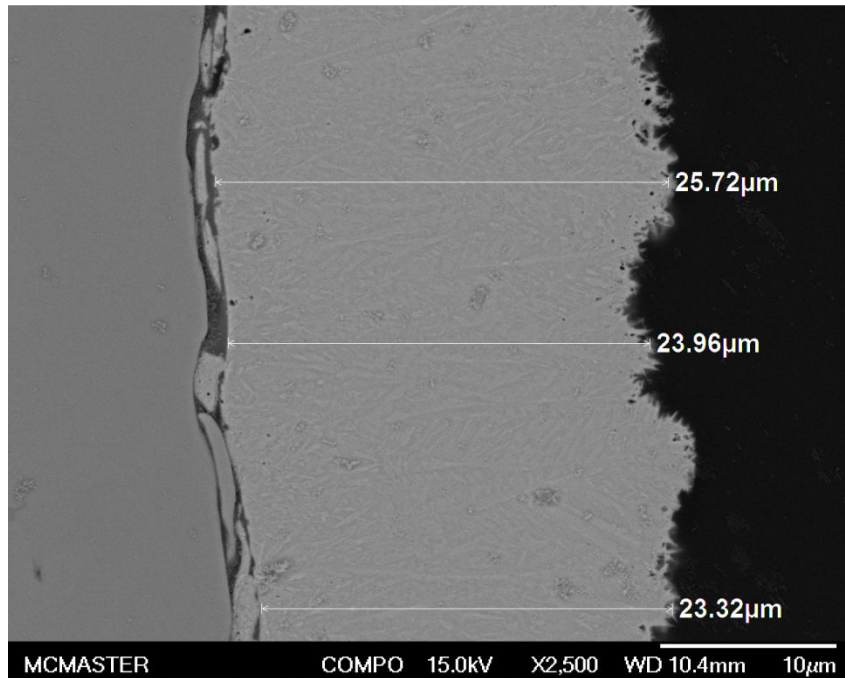


Figure 5-6: Cross-section of a cobalt coating plated from 1.3 M CoCl_2 + 0.5 M boric acid.

Samples produced by similar methods, but on stainless steel, were used to examine the surface of the non-oxidized cobalt coating. It was seen that dendrites preferably formed near the edges of the sample, as in Figure 5-7. These dendrites would cause high current densities, in addition to the usual edge effects, during manganese plating. Here, burnt manganese would likely occur. At the center, the morphology was no longer a dendritic structure.

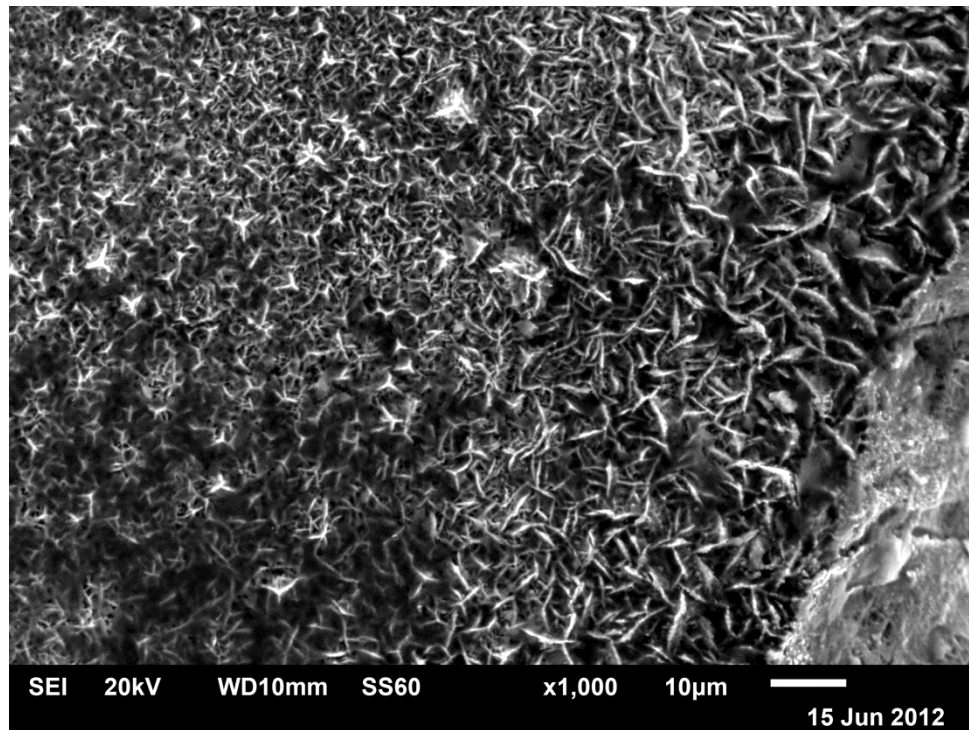


Figure 5-7: Top-down view of a cobalt coating plated from 1.3 M CoCl_2 + 0.5 M boric acid near sample edge.

Figure 5-8 shows a relatively smooth nodular structure. These samples exhibited a more uniform current density, but substantially lower than those of the dendrites. It is possible that the current density in this area is too low to promote manganese deposition. Between the central smooth deposit, and the sharp edge dendrites, a rough nodular surface was

found. This area is seen in Figure 5-9, where larger nodules protrude from the cobalt coating. These nodules, being closer to the anode than the rest of the plate, receive preferential deposition. Additionally, since they have a smoother surface than dendrites, they are less likely to cause sharp peaks in current density, and will form the wanted manganese coating. Between this rough nodular surface, and the dendritic area around the edge, there is a small transition section. Figure 5-10 shows this area, where dendrites transform to nodular growth. This band was narrow, only about 50 microns across.

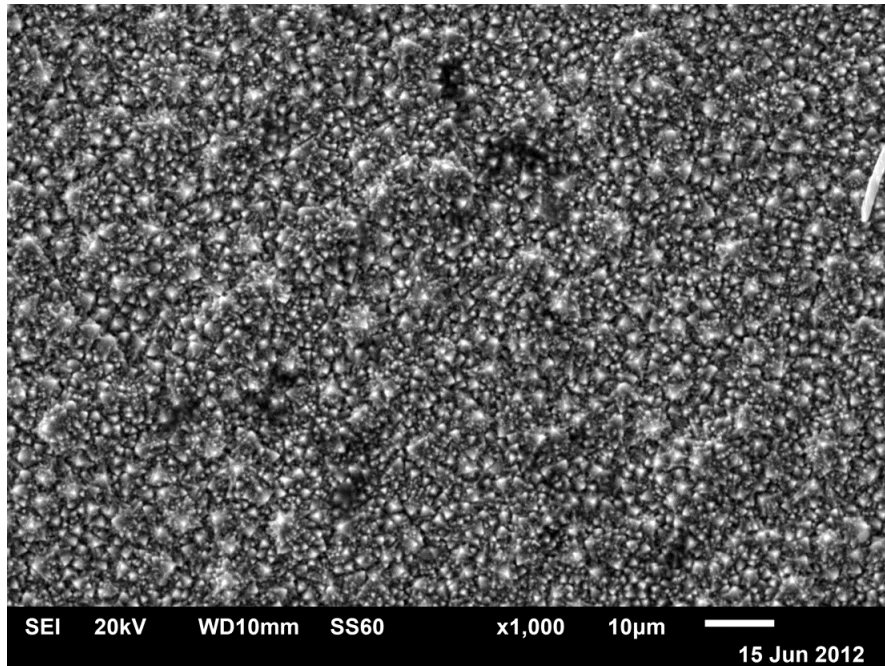


Figure 5-8: Top-down view of a cobalt coating plated from 1.3 M CoCl_2 + 0.5 M boric acid at sample center.

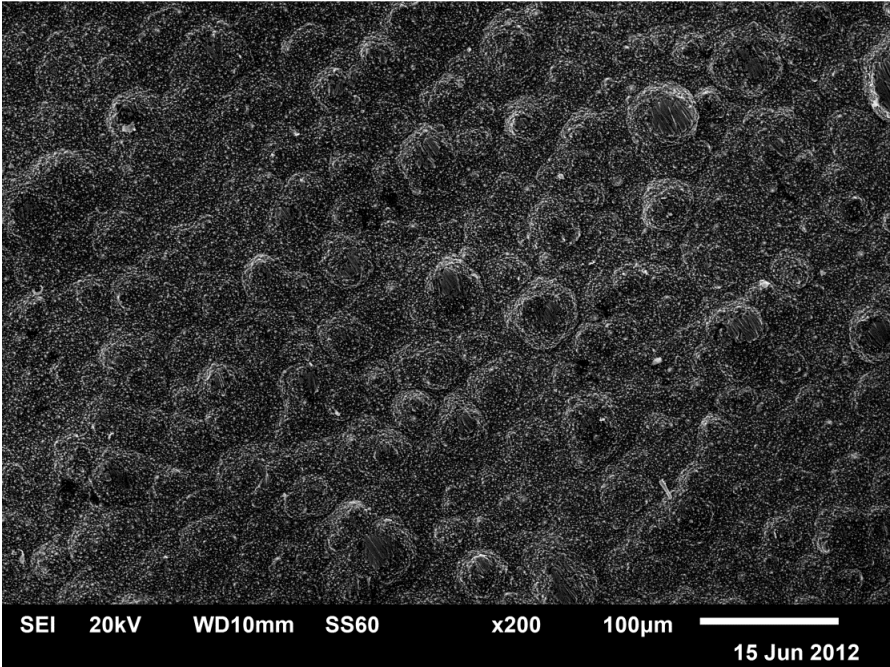


Figure 5-9: Top-down view of a cobalt coating plated from 1.3 M CoCl_2 + 0.5 M boric acid at transition from edge to center.

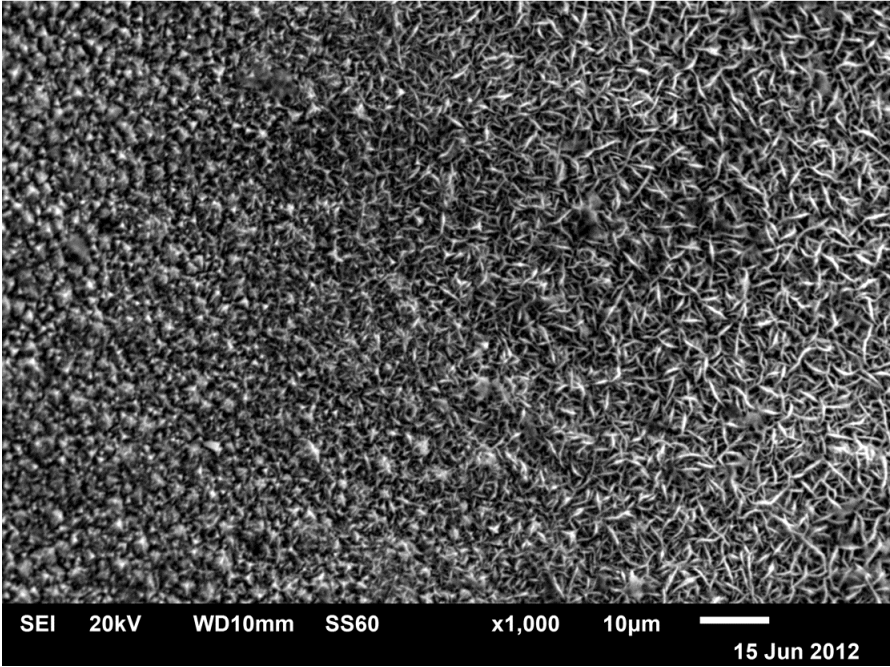


Figure 5-10: Top-down view of a cobalt coating plated from 1.3 M CoCl_2 + 0.5 M boric acid at nodular-dendritic transition.

In an attempt to remove this range of morphology, the process was repeated with an additional step. Once the coating was fully deposited, a short electropolishing step was performed. This simply required the polarity of the cathode and the anode to be reversed for 90 s, at the same current density applied for deposition. The resulting coating was metallic silver. This was cause for excitement, since a reflective surface was generally indicative of a smooth surface. Unfortunately, SEM imaging shows that although the surface was smooth, it was now fully dendritic, as seen in Figure 5-11. This process did not increase the success rate of manganese deposition. The electropolishing step was repeated in a solution of 10% sulfuric acid, with no improvement in success rate.

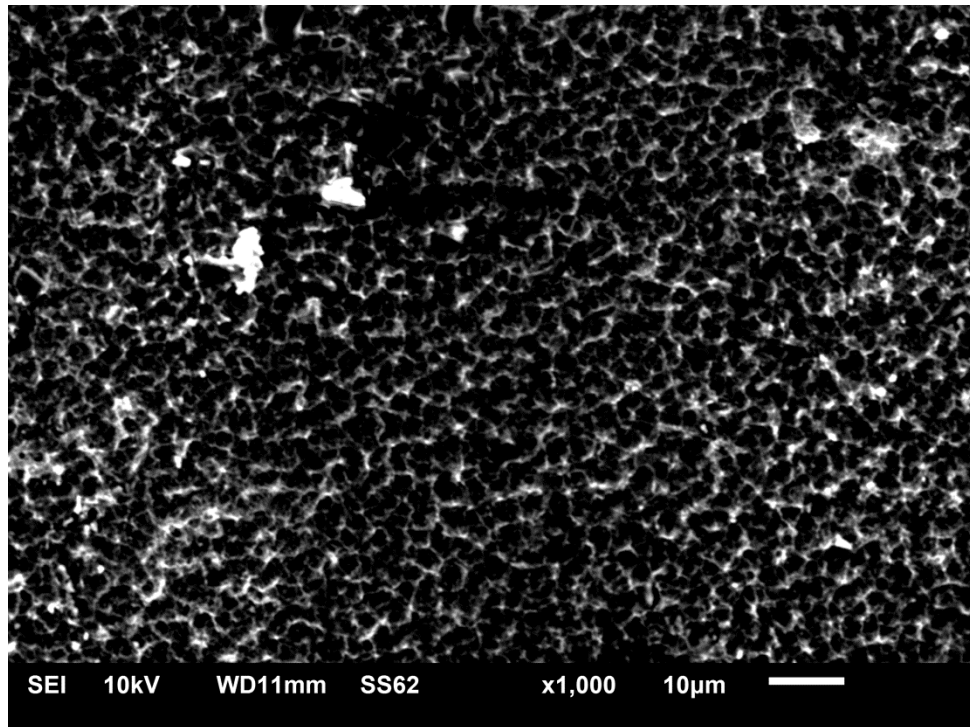


Figure 5-11: Top-down view of dendrite occurrence in cobalt deposit after electropolishing step. Plated in 1.3 M CoCl_2 .

After literature was revisited, it was found that the initial cobalt concentration of the solution was 400% that of standard industry solutions. A new solution was prepared, with a concentration of 0.32 M cobalt chloride, and 0.15 M boric acid. This solution now produced silvery metallic coatings. These new coatings were able to sustain manganese deposition with an almost perfect success rate. Figure 5-12 shows the smooth and even coating which starts at the edge. This smoothed morphology continues throughout the plate, which can be seen in Figure 5-13. The entire surface seems to be a distribution of small micron sized nodules. This would allow for the current density during manganese plating to remain constant, except near the edges.

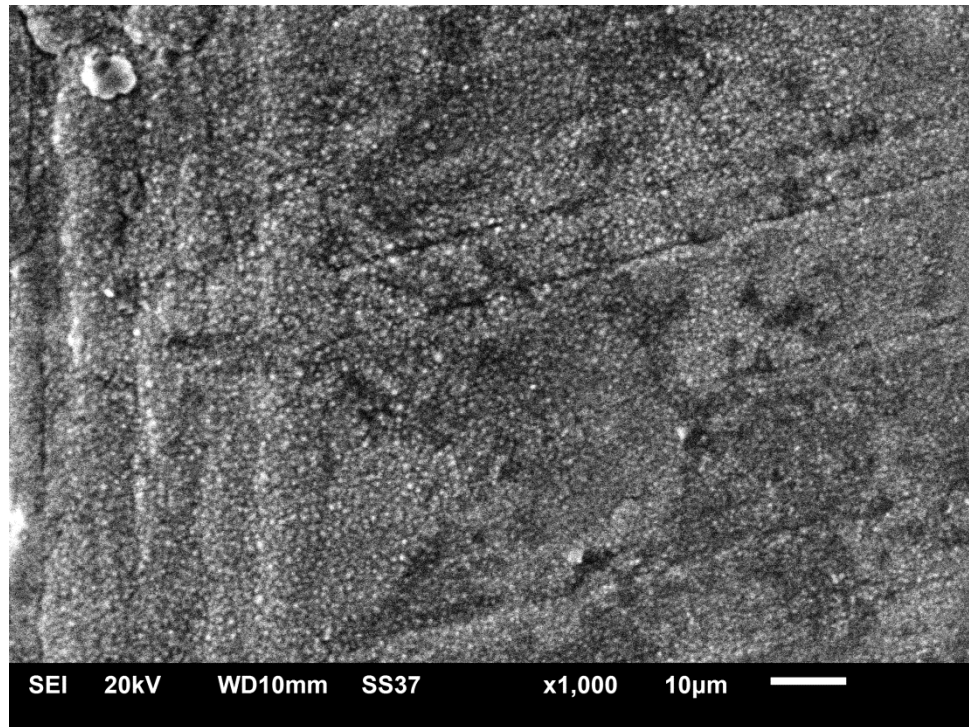


Figure 5-12: Top-down view of a cobalt coating plated from 0.32 M CoCl_2 near sample edge.

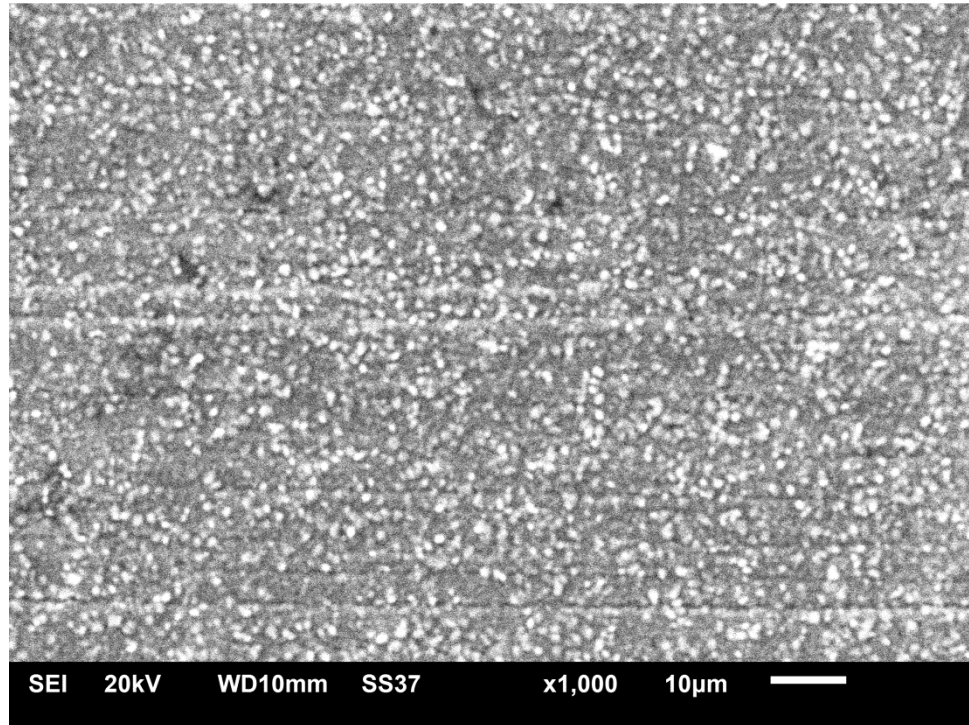


Figure 5-13: Top-down view of a cobalt coating plated from 0.32 M CoCl_2 at sample center.

Cobalt deposits from higher pH solutions would spall more readily than those at lower pH. However, the deposition process with high starting pH would quickly stabilize to a more sustainable pH value during deposition. Table 5-2 shows this trend. The pH was not tested in alkaline ranges, since cobalt oxides or hydroxides would precipitate immediately. Additionally, the pH was not reduced below 1.0, since no detrimental effects were observed near this limit. The cell operated well with a pH below 3.0, but the pH seemed to degrade at a lesser rate when the starting pH was less than 2.30. This buffering effect makes cobalt highly resistant to pH variations during plating, allowing for repeatability of results.

Table 5-2: Effects of bath starting pH on cobalt coating cohesion.

<i>Starting pH</i>	<i>Ending pH</i>	<i>Coating Quality</i>
6.23	2.86	Non-coherent
4.97	2.64	Non-coherent
4.18	2.62	Non-coherent
2.98	2.38	Coherent, Uniform
2.30	2.26	Coherent, Uniform
1.80	1.74	Coherent, Uniform
1.15	—	Coherent, Uniform



Figure 5-14: Smooth metallic cobalt coating obtained from a pH 2.30 solution.

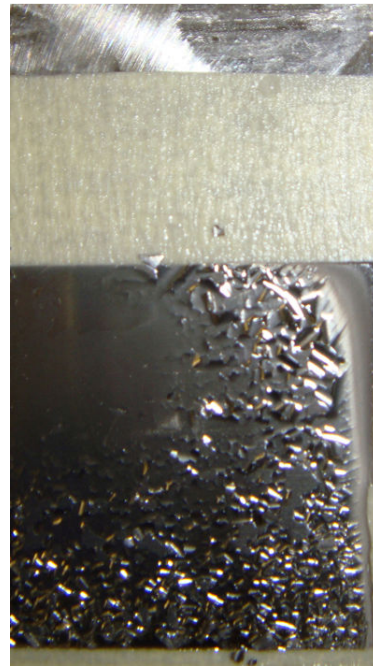


Figure 5-15: Damaged, but metallic, cobalt coating obtained from pH 6.23 solution.

Manganese Deposition

Manganese deposition was the most difficult process to optimize. In cases where the anode and anode were in the same solution, oxidation of manganese (and impurities) occurred at the anode surface. This had potential detrimental effects since this coating could detach from the anode and enter the solution. Additionally, these oxides formed an

insulating coating on the anode, wasting power. Should these oxides reach the cathode, they could co-deposit with manganese metal, causing inclusions. Additionally, these oxides had to be filtered out, wasting solution metal content. The simplest method to prevent these side reactions is to place the anode in an anolyte which is separated from the catholyte by a diaphragm. Although this was easily done for small samples, using a glass frit, it becomes exponentially more expensive to install glass frits large enough for industrial plates. Since separating anolyte and catholyte was not an option, an anode bag was used to capture the detached oxides, preventing them from reaching the cathode. Although this did not avoid losing metal from the solution, it did prevent the entrapment of inclusions at the cathode. The black residue (when dried) was collected and analyzed by XRD and SEM-EDS which showed that the powder was mainly manganese oxide, with impurities of iron and sulfur. These impurities are estimated to be less than 10 ppm for iron, and 60 ppm for sulfur. The sulfur was likely adsorbed manganese sulfate solution dried within the anode deposit. Iron likely came from the natural impurities of the solution. The EDS signal indicated the oxygen-to-manganese ratio to be around 2:1. This corresponds to a form of MnO_2 , which is consistent with the Pourbaix diagram for aqueous manganese. Additionally, the anode remained electrically conductive during electroplating even when covered. Manganese (IV) oxide was, at least partially, conductive at room temperature.

Unlike all the other solutions used in this thesis, manganese required a much narrower range of pH to deposit satisfactorily. The pH of the solution at the start of the deposition process was set to 3.3 ± 0.1 . This value would quickly drop as plating times increased. The

solution would need to be neutralized by a 10% NH_4OH solution, such that the pH would return to the desired value. Starting the deposition process outside of the marked pH range would provide incomplete coatings, or in the case of very low pH values, no coating at all.

The design of interconnect plates had a strong effect on the deposition of manganese. The two gas ports, seen in Figure 5-16, were associated with substantial defects in the manganese coating. Since the top hole was masked, its effect was minimal. However, the lower was not. Here, the edge effects caused by the hole prevented the application of an even manganese layer. By masking the lower hole, the edge effects were diminished, seen in Figure 5-17.



Figure 5-16: Edge effects at lower hole when Mn was plated at $70 \text{ mA}\cdot\text{cm}^{-2}$ on cobalt coated chromium.

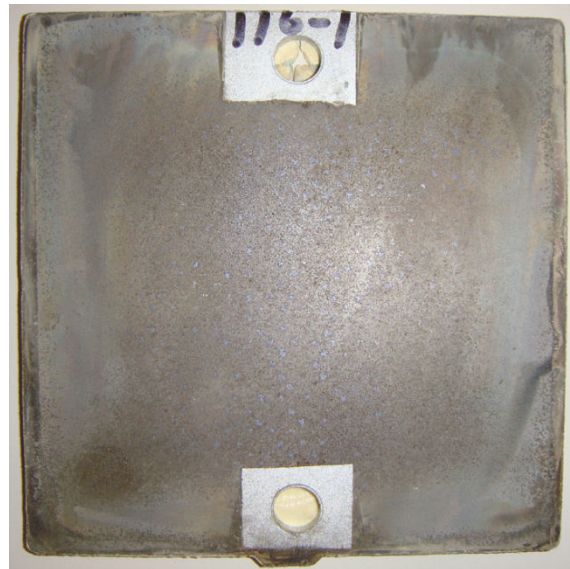


Figure 5-17: Lack of edge effects at lower hole when Mn was plated at $70 \text{ mA}\cdot\text{cm}^{-2}$ on cobalt coated chromium with additional mask.

The effects of the cathode current density were profound for manganese plating. Not only was the cathode current efficiency strongly controlled by the current density, but so also were the coating morphology and the size of the burnt edge effect. The effects of current densities between 40 and 110 mA·cm⁻² were tested for cobalt coated industrial sized chromium plates. The edge effects found on large plates were substantial for any plate coated at current densities higher than 70 mA·cm⁻². The plates in the figures above had edge effect bands with an average width close to a quarter centimeter. Plates coated at 110 mA·cm⁻² had a band that was nearly a half centimeter in width. Manganese plated at 40 mA·cm⁻² resulted in a decreased band width of less than a millimeter, except at the corner, where it ranged from 1 to 1.5 mm. Excluding the area affected by edge effects, the overall quality of the manganese coating was consistent for the full range of current densities examined. The anode in all cases was an 8 cm by 10 cm platinum plate. Approximately 1 cm of the anode length was suspended above the solution, to prevent the electrical clamp from dissolving into the solution.

The manganese surface was imaged prior to oxidation, to qualify the coating at the center and in the edge affected zones. While both the center and edges were manganese rich, the bonding at the edges was weak, and could be removed by wiping with a cloth. Figure 5-18 shows the transition of the manganese coating from the edge affected zone to the center.

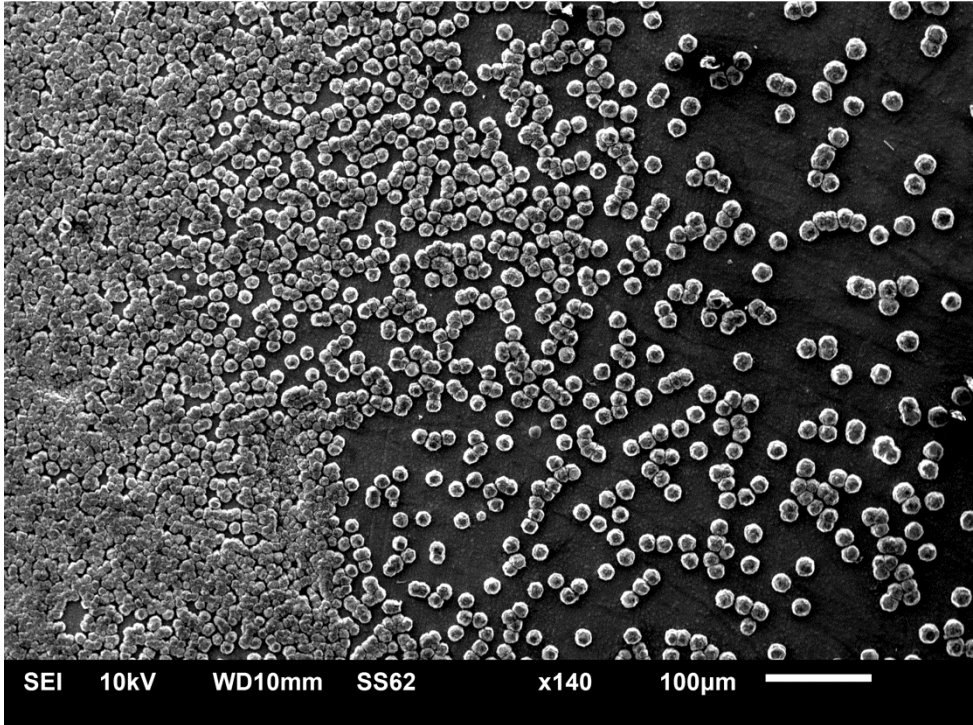


Figure 5-18: Transition from "burnt" to thick manganese coating.

The edge affected area, on the right, was both thin and glossy. At increasing coating distance from the edge, the amount of manganese increased, forming the continuous coating shown in Figure 5-19. The coating in the center of the deposit became more compact, showing no exposed cobalt. The grain size also had been refined, dropping from around 10 microns at the transition area to about 7 microns in the center.

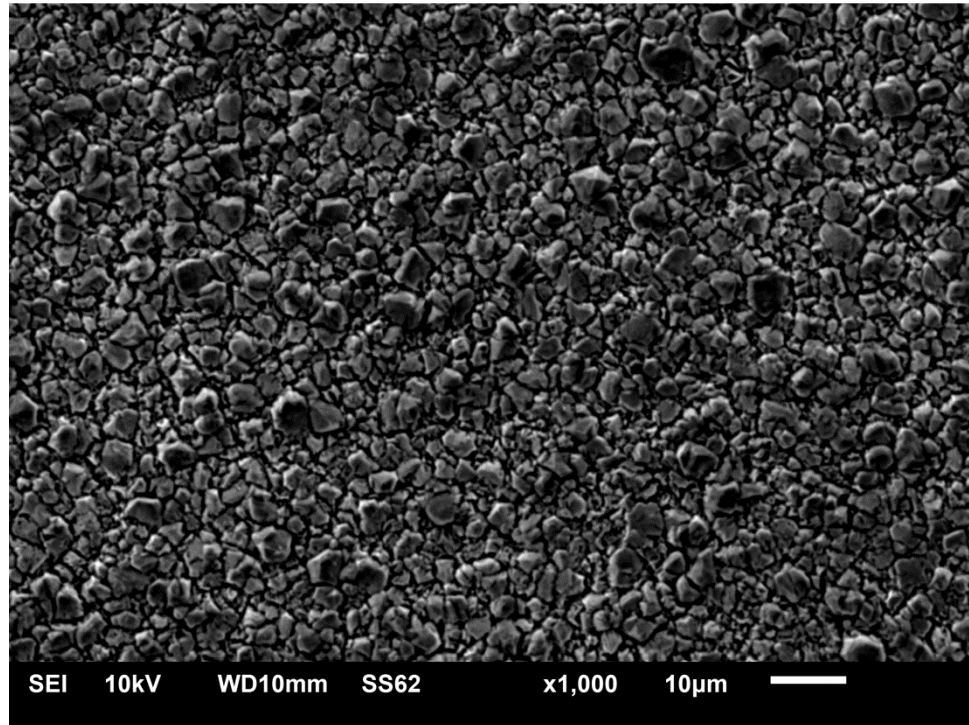


Figure 5-19: Continuous manganese found at the center of a deposit.

Selenium dioxide is commonly used in industry to increase the cathode efficiency during plating of manganese. However, impurities of selenium reduce corrosion resistance, and may cause other problems in fuel cell coatings. However, the benefits in electrodeposition are seen even when low levels of the additive were included in the solution. Additions of 2 mg per liter of selenium dioxide increased the cathode current efficiency by around 5% by reducing the overall hydrogen evolution reaction. At this concentration, the inclusions of selenium within the coating were less than 50 ppm per minute of plating time.

Lastly, experiments were done with the addition of hydroxylamine hydrochloride. It has been reported that $\text{NH}_2\text{OH}\cdot\text{HCl}$ is useful in the prevention of oxides in the solution, and

that it reduces the evolution of hydrogen at the cathode. The first observation made using this new solution was that the anode deposit was substantially thinner, and less adherent. It could easily be dissolved within the manganese solution, such that little or no material was lost during filtration. Additionally, hydrogen bubbles were found to move away from the cathode at a faster rate than solutions without the additive. The manganese deposit also became more stable, dissolving at a lower rate while the cathode remained in the solution without an applied current. The behaviour of the manganese, when using hydroxylamine hydrochloride, was different depending on the underlying coating. While plating manganese on copper, the deposits were even and uniform, seen in Figure 5-20. On cobalt however, new defects began to arise. These would form areas of burnt manganese, or simply bare cobalt, near the top right of the coating. This is seen in Figure 5-21.



Figure 5-20: Manganese deposited on Cu with $\text{NH}_2\text{OH}\cdot\text{HCl}$.

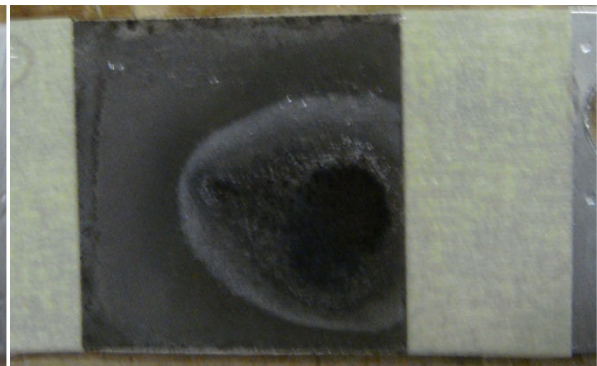


Figure 5-21: Manganese deposited on Co with $\text{NH}_2\text{OH}\cdot\text{HCl}$.

The defects found on cobalt-manganese coatings were intensified as the surface area of the plates increased. On cobalt-coated industrial plates, manganese could not be plated using a solution containing hydroxylamine hydrochloride.

Coating Composition Results by ICP

Coatings of different compositions were tested by ICP to further quantify the composition of current electrodeposited coatings. After deposition, the coatings were mechanically removed from the stainless steel substrate and dissolved in acid. Table 5-3 shows the results of the ICP testing.

Table 5-3: Results of ICP performed on different coatings.

	Sample #1 [Ni-Cu-Mn]			Sample #2 [Co-Mn]			Sample #3 [Co-Cu-Mn]		
	Plating Time (s)	Mass Gain (mg)	CE (%)	Plating Time (s)	Mass Gain (mg)	CE (%)	Plating Time (s)	Mass Gain (mg)	CE (%)
Ni	37	1.7	93	—	770 ppm	—	—	820 ppm	—
Co	—	1,000 ppm	—	987	22.9	61	731	12.0	42
Cu	199	17.3	89	—	1,100 ppm	—	95	6.9	88
Mn	313	30.2	56	185	13.6	48	183	13.5	49
Common Impurities									
Fe	—	160 ppm	—	—	720 ppm	—	—	840 ppm	—
Se	—	260 ppm	—	—	150 ppm	—	—	180 ppm	—

There are several important features in the ICP tests. First, the impurity levels in the coating can be quite substantial. Samples showed elevated levels of co-deposited iron, cobalt, copper, and nickel in cases where they were not intended. It is likely that these impurities come from any of the baths used, but the main cause remains the same. Initial impurity levels of solutions, combined with the insufficient rinsing procedures can cause co-deposition to occur. Although it is unknown if these levels of impurities will be detrimental to the coatings during operation, they do have an effect during deposition. The current efficiency for the deposition of a certain metal drops when co-deposition occurs. This has the effect of shifting the final composition of the spinel coating in an unpredictable direction. For examples, while manganese and nickel had current

efficiencies near their expected values, cobalt and copper were at least 10% less. This resulted in coating #3, intended to be a $\text{Cu}_{0.5}\text{MnCo}_{1.5}\text{O}_4$ spinel, to have a composition of $\text{Cu}_{0.6}\text{Mn}_{1.3}\text{Co}_{1.1}\text{O}_4$. Additionally, these coatings were much thinner than expected, with an average thickness of $7\ \mu\text{m}$, rather than $10\ \mu\text{m}$.

6. Oxidation of Metallic Coatings

Selected spinel coatings were oxidized for imaging and characterization. All coatings were subjected to the same oxidation process, which included air as the oxidizing gas, the heating and cooling rates, and the reaction temperature. Some coatings were oxidized for shorter periods of time to determine the progress of the oxidation and chromium penetration. Two primary compositions of spinel coating were investigated; cobalt-manganese and nickel-copper-manganese. Table 6-1 is a tabulation of the samples presented in this thesis. These show the wide range of spinel compositions that can easily be coated on either chromium or stainless steel samples. The expected composition was defined by the plating time of each element, taking into account current efficiencies, to produce a 10 micron metallic coating. Each spinel coating was plated in the following sequence: Co-Cu-Mn, or Ni-Cu-Mn.

Table 6-1: Investigated spinel samples.

Cobalt-based Spinel				Copper-based Spinel			
Sample ID #	Expected Spinel	Substrate	Oxidation Time (hrs)	Sample ID #	Expected Spinel	Substrate	Oxidation Time (hrs)
114-1a	Mn ₁ Co ₂ O ₄	Cr-5Fe	120	117-1	Ni _{0.5} Cu _{0.7}	Cr-5Fe	120
114-1b		430 SS		121-3	Mn _{1.8} O ₄	430 SS	
114-2a	Mn ₁ Co _(2-Disp)	Cr-5Fe		117-2	Ni _{0.1} Cu _{0.7}	Cr-5Fe	
114-2b	Cu _{Disp} O ₄	430 SS		121-1	Mn _{2.2} O ₄	430 SS	
114-3a	Mn ₁ Cu _(0.5+Disp)	Cr-5Fe		118-2	Ni _{0.1} Cu _{1.1}	Cr-5Fe	
114-3b	Co _(1.5-Disp) O ₄	430 SS		121-2	Mn _{1.8} O ₄	430 SS	
124-3	Mn ₁ Co ₂ O ₄	Cr-5Fe	24	124-1	Ni _{0.1} Cu _{0.7}	Cr-5Fe	24
124-4	Mn ₁ Cu _(0.5+Disp)			124-2	Ni _{0.1} Cu _{1.1}		
	Co _(1.5-Disp) O ₄				Mn _{1.8} O ₄		

In certain samples, Cu_{Disp} denotes that copper was not electroplated, but was obtained on the cobalt by displacement reaction. This removed some cobalt from the spinel system, although the extent of the cobalt dissolution was not known. The copper was applied by spraying the cobalt surface for 2 seconds with 0.2 M cobalt sulfate solution using a 2 mm diameter stream placed above the coating.

Chromium substrates are widely used in SOFCs which causes a new phenomenon to be observed in these samples. Nitrides formed at the interface between the spinel and metal surface. This nitride phase grew with oxidation time, and may be the cause of some coating damage. Although the occurrence of the nitride phase was not of direct interest in this thesis, it had an effect on coating integrity.

Appendix A contains 12:1 aspect ratio images of many coatings, taken at a low magnification. These SEM images are those used to determine the quality of a 600 micron wide portion of the coating, while keeping a magnification of x500. The substrates have an average width of 2.2 cm, and therefore these images only show 3% of the cross-section. These are labelled by the identification (ID) numbers found in Table 6-1.

Cobalt-Manganese (MnCo_2O_4) Spinel Coating

The MnCo_2O_4 spinel has been identified as the most conductive spinel on the cobalt-manganese system. Both cobalt and manganese metal coatings are said to have good chromium retention. Therefore, this spinel should be ideal as an interconnect coating. It was coated on both stainless steel and chromium substrates. Imaging of this spinel on

stainless steel substrates which were oxidized for 120 hours showed a nearly uniform layer. This coating was well adhered, with no gap, crack or defect between layers, as seen in Figure 6-1. There are a few interesting points to note. First, the area between the dense spinel on the left and the 1 micron thick chromia scale was porous. This was common in most coatings, and was probably due to a structure mismatch. The spinel structure in this area had high levels of iron impurities, determined by EDS. This substantial amount of iron, diffused through the structure from the substrate, could also cause this porosity. Additionally, there was some material (cobalt) that was trapped behind the chromia scale. However, this was an anomaly only found in one location. Examination of the wide-image shows no other deposit of non-reacted material. This was an entirely different situation from the chromium substrate.

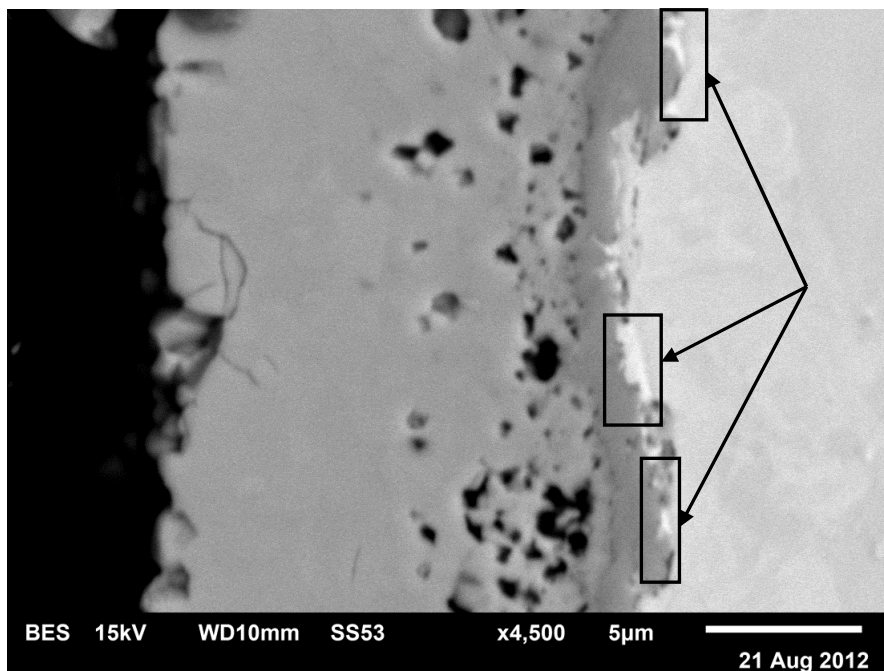


Figure 6-1: MnCo_2O_4 on stainless Steel after 120 hours (ID 114-1b).

After 24 hours of oxidation, much of the coating on the chromium substrate has not reacted. The low resolution image demonstrates this clearly. Large deposits, approximately 2.5 microns thick, of cobalt metal were found along the surface, but behind a chromia scale which was less than 1 micron thick. Additionally, surface damage due to nitrides could already be seen in Figure 6-2. This damage was in the form of small crystalline material behind the unreacted cobalt. The metallic cobalt phase was a solid solution with chromium.

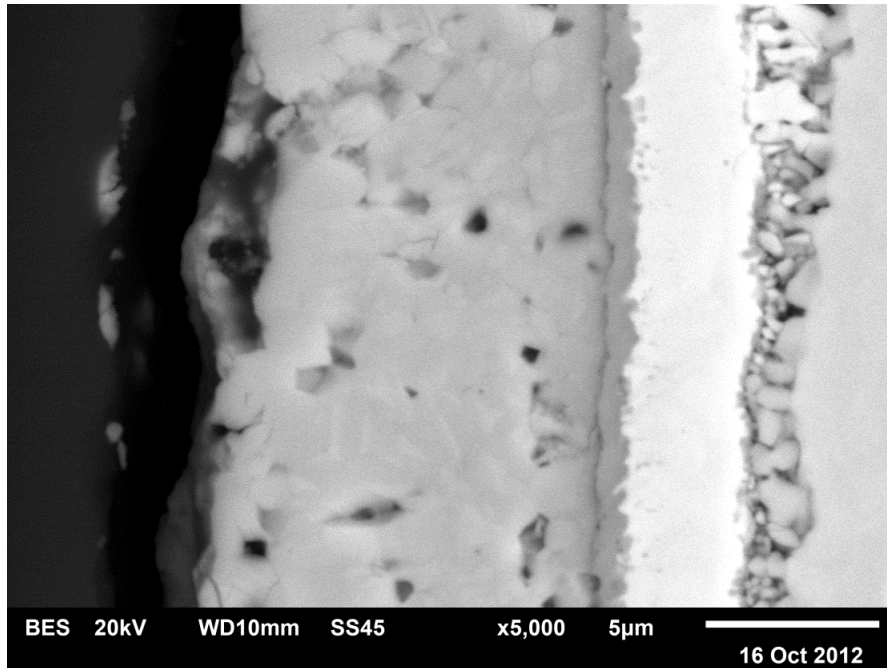


Figure 6-2: MnCo_2O_4 on Cr-5Fe substrate oxidized for 24 hours (ID 124-3).

EDS analysis showed this phase to be at a 2:1 cobalt to chromium molar ratio. Otherwise, the spinel coating seemed to have better adhesion to the chromia scale, since the porosity was much lower. However, the spinel was not of the expected composition, since some of the cobalt was retained in metallic form behind the chromia. Results of EDS measurements taken in the spinel showed that cobalt had a quarter of the expected

concentration. This would constitute a spinel near the CoMn_2O_4 stoichiometry. This spinel is expected to be about ten times less conductive. The chromium content within the spinel near the metal interface was elevated. Increasing amounts of chromium in the spinel lattice substantially increase the resistance of the coating. However, unlike the stainless steel sample, there is virtually no iron within the coating.

The surface and coating of cobalt-based spinel deposits are further degraded as oxidation times increased to 120 hours. The chromia scale grew to about 3 microns in thickness, and the nitride layer had further fragmented. As such, the coating now had extensive damage, and could easily be separated from the substrate, as seen in the low magnification image. Although Figure 6-3 gives the impression that the cobalt-chromium metal solution had grown, it is simply a larger deposit than that of Figure 6-2. The overall coating showed a reduction in the number and size of trapped metal deposits. EDS showed that the spinel structure adjacent to the chromia scale had more cobalt content than that of the 24 hour oxidation. The spinel composition, according to EDS analysis, would be close to $\text{Mn}_{1.5}\text{Co}_{1.5}\text{O}_4$. The chromium and iron contents however, remained the same as before. This would indicate that an oxidation time of greater than 120 hours would be needed to completely convert the metallic coating.

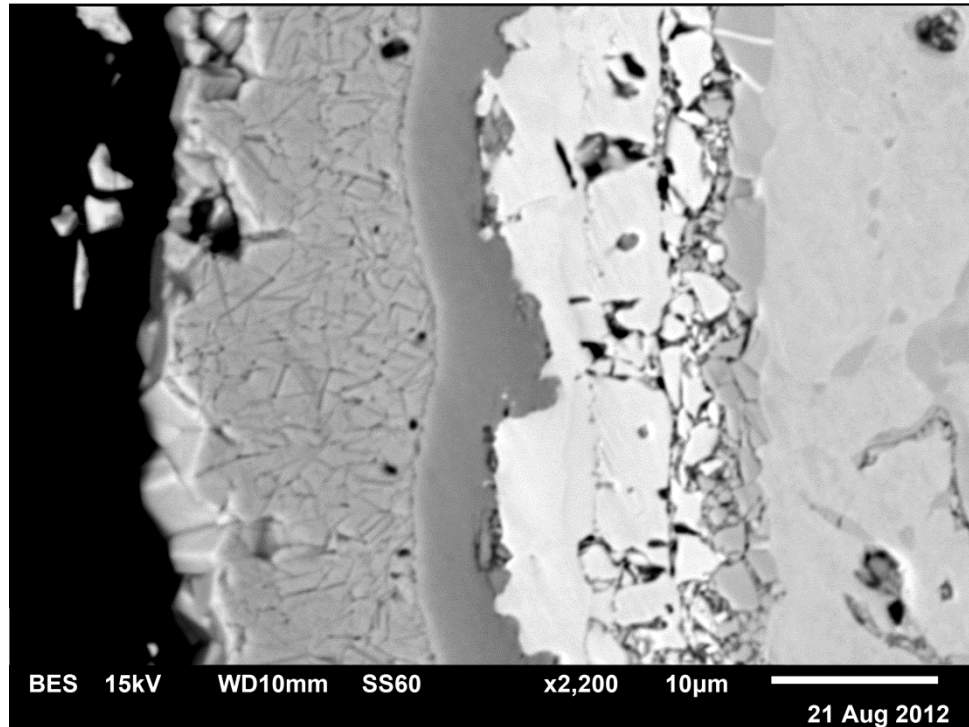


Figure 6-3: MnCo_2O_4 on Cr-5Fe substrate oxidized for 120 hours (ID 114-1a).

Cobalt-Manganese ($\text{MnCu}_{\text{Disp}}\text{Co}_{(2-\text{Disp})}\text{O}_4$) Spinel Coating with Thin Copper Interlayer

The results for this set of samples were predictable. Since the amount of cobalt displaced, and the amount of copper deposited were expected to be a fraction of total mass of the coating, these samples were expected to be similar to a pure cobalt-manganese spinel. The results from the low magnification image were similar to those found without copper. For stainless steel samples, the coating was mostly well adherent, with some porosity. The spinel structure had been infiltrated by a minimal amount of chromium, but significant concentrations of iron. In the chromium sample, the thick deposits of cobalt-chromium solution protected by chromia scale were still present. When EDS was performed on the coating of chromium samples, it was only able to detect minor impurities, if any at all. Therefore, there were no appreciable structural or chemical

differences caused by adding the copper interlayer. The ease of application however, an important consideration, was improved. Adding the copper interlayer ensures that manganese can be deposited on chromium, regardless of the cobalt surface condition.

Cobalt-Copper-Manganese ($\text{MnCu}_{(0.5+\text{Disp})}\text{Co}_{(1.5-\text{Disp})}\text{O}_4$) Spinel Coating

The spinel containing 17% copper behaved differently than those without the additions. In stainless steel, a segregation of copper was found between the chromia scale and substrate. In Figure 6-4, the boxed area shows the formation of a different phase. This is not chromia, but a chromium-rich manganese oxide with high concentrations of copper.

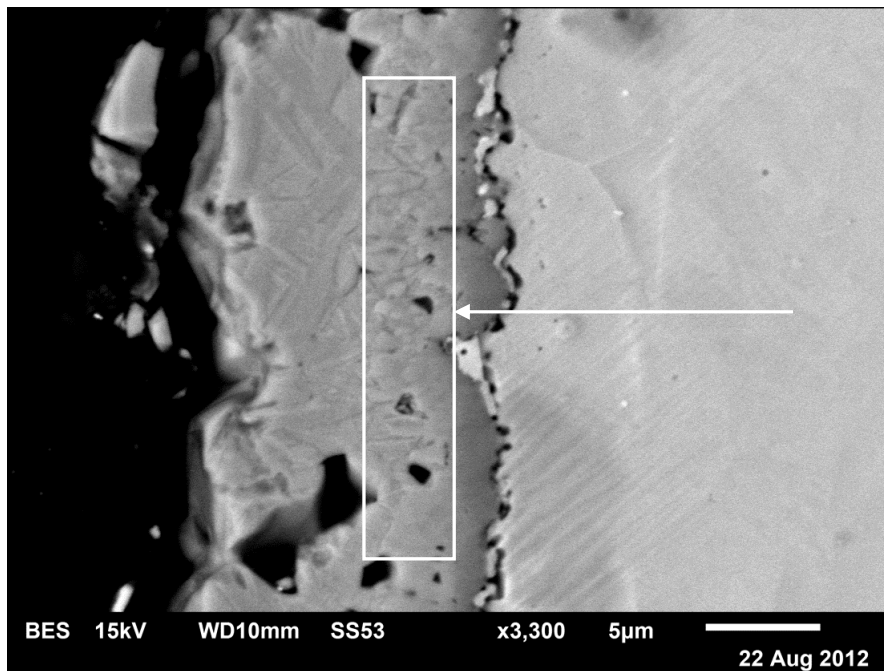


Figure 6-4: $\text{MnCo}_{(1.5-\text{Disp})}\text{Cu}_{(0.5+\text{Disp})}\text{O}_4$ on 430 SS substrate oxidized for 120 hours (ID 114-3b). The box and arrow highlight a chromium-rich spinel formed in the coating.

The majority of the cobalt is found in the segregated metal, and at the free edge. Some of the cobalt was actually found inside the substrate, just below the interface. Another

difference between these samples and the ones that contain little copper was the porosity at the chromia-steel interface. This indicates that the coating might fail faster than low-copper cobalt coatings.

On the chromium substrate, the coating behaved similarly to coatings that contained no copper. After 24 hours of oxidation, large deposits of metallic cobalt could be found. This deposit was no longer simply cobalt and chromium, but had copper in solution at the cobalt-chromia interface. The dense spinel had the expected composition, with slight chromium impurities. There were only slight variations of composition from the free interface up to the chromia phase. Figure 6-5 shows a coating pattern similar to that found in Figure 6-2. However, the nitride formation was a single continuous phase that had detached from the substrate.

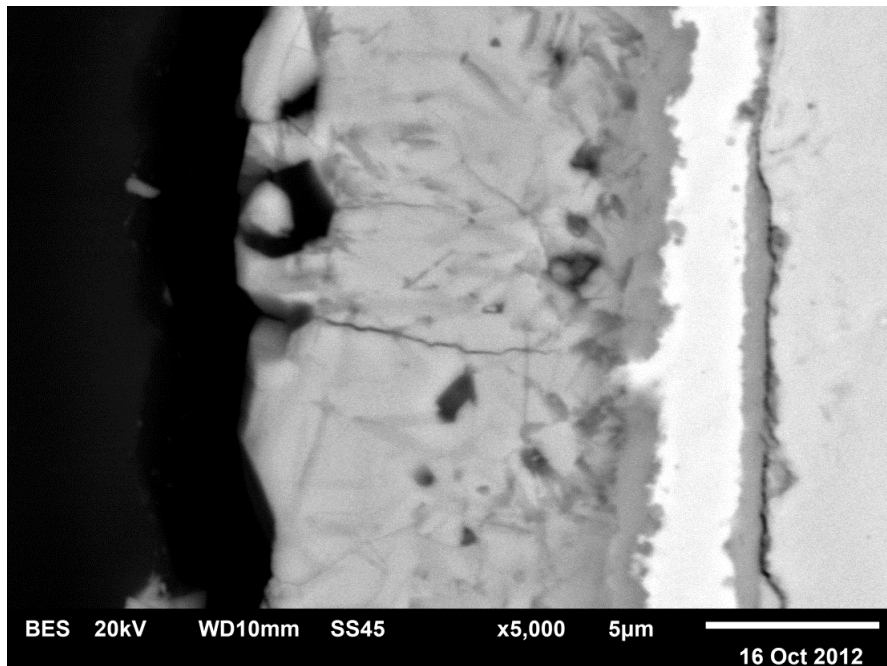


Figure 6-5: $\text{MnCo}_{(1.5\text{-Disp})}\text{Cu}_{(0.5\text{+Disp})}\text{O}_4$ on Cr-5Fe substrate oxidized for 24 hours (ID 124-4a).

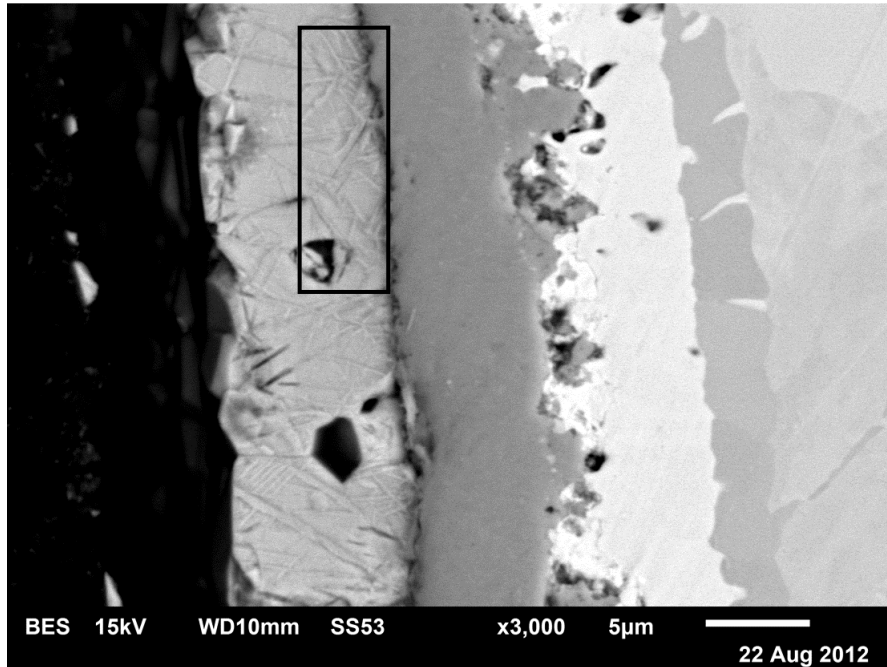


Figure 6-6: $\text{MnCo}_{(1.5\text{-Disp})}\text{Cu}_{(0.5\text{+Disp})}\text{O}_4$ on Cr-5Fe substrate oxidized for 120 hours (ID 114-3a). The section highlighted by a box emphasizes dendrite formation in the spinel structure.

Oxidizing this coating for 120 hours resulted in behaviours similar to low-copper, cobalt-manganese spinels. Some of the metallic deposit entered the spinel, and stabilized the composition. It was seen, however, that the copper entered the spinel structure faster than cobalt, which left porous regions between the metallic cobalt and chromia. This phenomenon is seen in Figure 6-6. The wide-image showed this to be true for many of the deposits. The thickness of the chromia scale again increased from around 1 micron after 24 hours, to nearly 5 microns after 120 hours. The nitride formation was continuous, but did not lead to coating failure during processing. The dendrite structure found within the spinel, highlighted by the box, was of unknown origin. It has been encountered in different spinels, and shows little compositional variance.

Nickel concentrated Copper-Manganese ($\text{Ni}_{0.5}\text{Cu}_{0.7}\text{Mn}_{1.8}\text{O}_4$) Spinel Coating

The nickel-rich copper manganese spinel coatings had issues with adhesion on stainless steel. This was noted in the electrodeposition section, as thick nickel had substantial internal stresses. However, these coatings seemed to have acceptable adhesion. Higher magnification is given in Figure 6-7. It shows a mostly dense spinel structure with some porosity at the spinel-chromia interface.

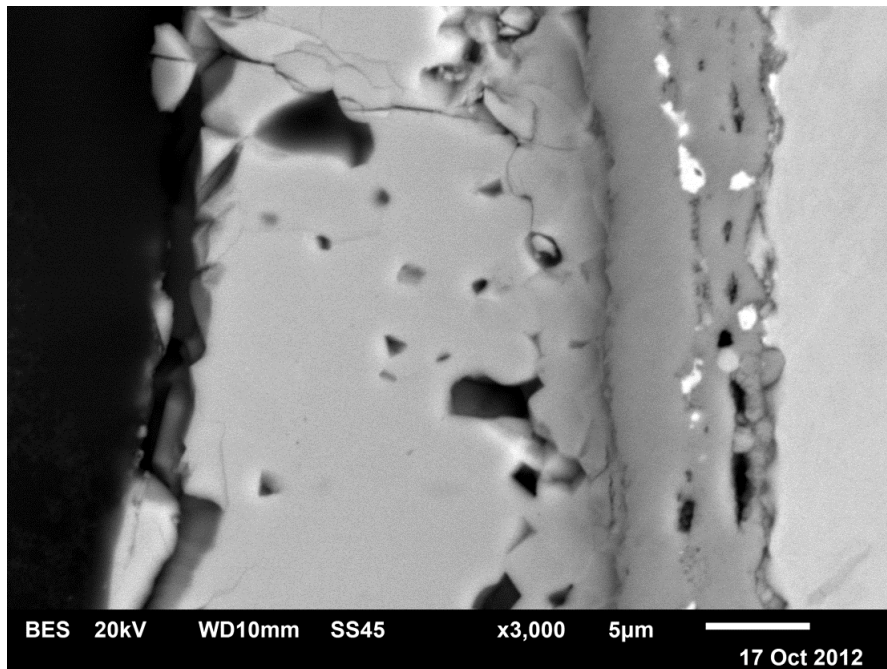


Figure 6-7: $\text{Cu}_{0.7}\text{Ni}_{0.5}\text{Mn}_{1.8}\text{O}_4$ spinel coating oxidized for 120 hours on Cr-5Fe (ID 117-1).

The spinel had the expected composition, with slight variation, and minimal chromium impurities. Also, behind and embedded in the chromia, some metallic copper deposits can be seen. These deposits are much smaller and sparser than in cobalt-based spinels. This can be seen in the low magnification image. Dissimilar from cobalt-based coatings, the nitridation of the substrate was much less apparent, sometimes undetectable.

High-Manganese Copper-Nickel ($\text{Ni}_{0.1}\text{Cu}_{0.7}\text{Mn}_{2.2}\text{O}_4$) Spinel Coating

Stainless steel samples with high concentrations of manganese do not form the spinel structure, but resulted in multiple phases. The copper diffused through the outer layer and formed a different oxide phase. In this area, highlighted in Figure 6-8, the composition was shifted to an even ratio of manganese and copper. The remainder of the coating was a two phase region on the phase diagram, where spinel and bixbyite are in equilibrium.

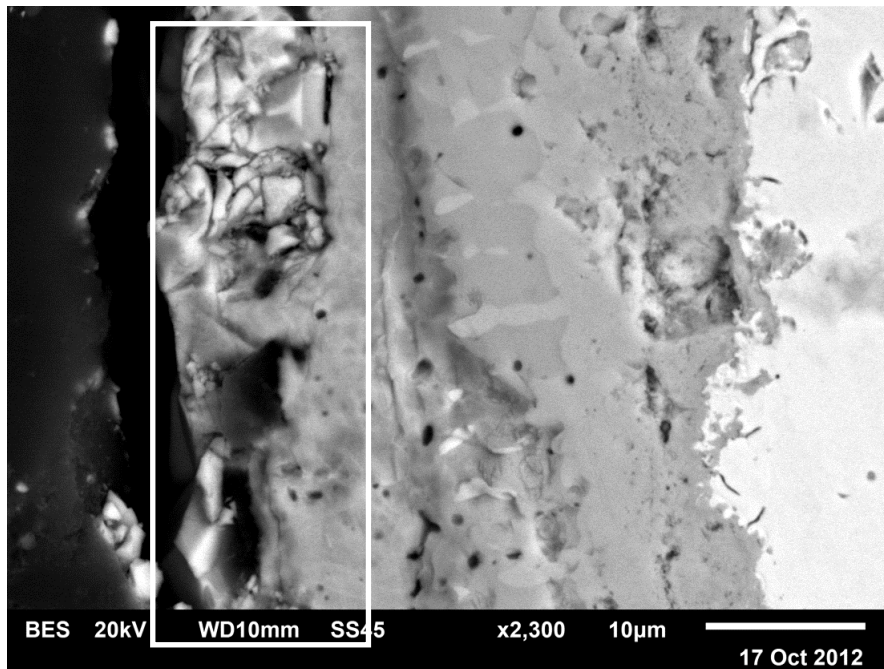


Figure 6-8: $\text{Ni}_{0.1}\text{Cu}_{0.7}\text{Mn}_{2.2}\text{O}_4$ spinel coating oxidized for 120 hours on 430 SS (ID 121-1). The box highlights the region rich with copper in the coating.

Directly under this region was a manganese rich oxide with impurities of iron. The remaining coating, except for the chromia scale, was a mix of iron, nickel and manganese oxides. The low magnification image showed an exceptionally strong adhesion, likely due to the invasive diffusion of iron throughout the coating. Additionally, the free

interface of the coating was highly damaged and porous. This was likely due to the high concentration of copper oxide.

The results of the chromium substrates were very different than those of stainless steel substrates. Copper was no longer condensed at the free interface, but rather formed a spinel with manganese. In both the 24 hour and 120 hour oxidation, chromium was present in low concentrations. There was increased chromium diffused into the spinel near the spinel-chromia interface. The coatings on chromium substrates showed better quality than those on stainless steel. After 24 hours, only small inclusions of metal copper could be found behind the chromia.

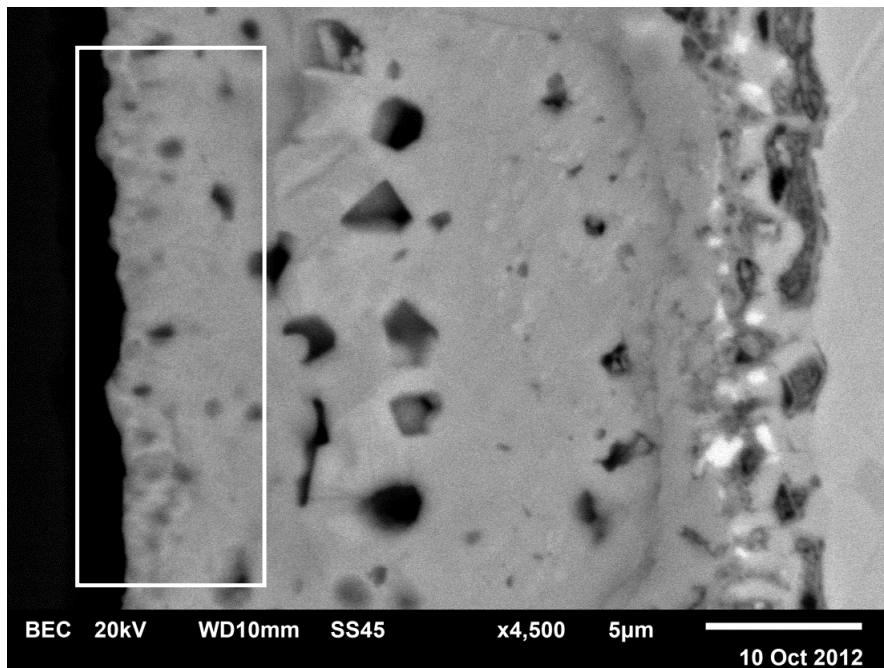


Figure 6-9: $\text{Ni}_{0.1}\text{Cu}_{0.7}\text{Mn}_{2.2}\text{O}_4$ spinel coating oxidized for 24 hours on Cr-5Fe (ID 124-1). Outlined area denotes a copper free manganese spinel phase.

The outlined section in Figure 6-9 was a copper-free manganese oxide. Directly adjacent to it was the expected copper-manganese spinel with porosity at the interface. Again, nitride formation behind the chromia can be seen. The structure and phase distribution of the coating after 120 hours of oxidation were almost identical to the 24 hour sample. Figure 6-10 showed that the primary difference between the samples was the increased thickness of the chromia scale. The low magnification images of the coatings show that there is a decrease in the amount of metal inclusions. They also show that the top-most layer of the coating degraded with longer oxidation time. After 120 hours, the manganese oxide section was porous, cracked, or missing.

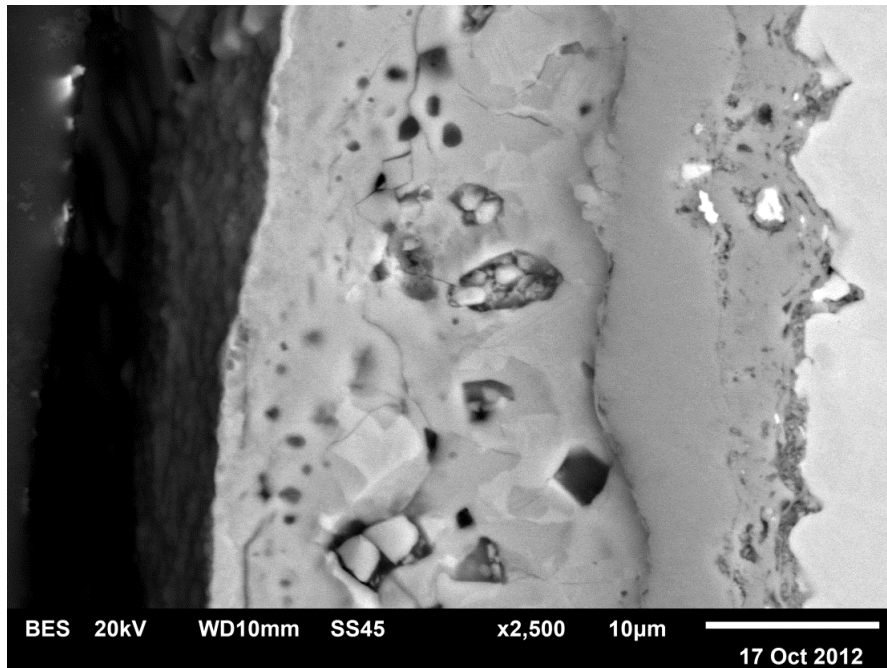


Figure 6-10: $\text{Ni}_{0.1}\text{Cu}_{0.7}\text{Mn}_{2.2}\text{O}_4$ spinel coating oxidized for 120 hours on Cr-5Fe (ID 117-2).

Copper-Nickel-Manganese ($\text{Ni}_{0.1}\text{Cu}_{1.1}\text{Mn}_{1.8}\text{O}_4$) Spinel Coating

This copper-nickel-manganese spinel composition formed an exceptionally well adherent coating on stainless steel samples. The spinel formed with little compositional gradient and low chromium content. However, like most spinel coatings, the iron infiltrated the structure quite readily. In Figure 6-11, and in the low magnification image, there were only three phases present; the substrate, the chromia scale, and the spinel. Of the nickel-copper spinels, this was the only composition which yielded a usable coating.

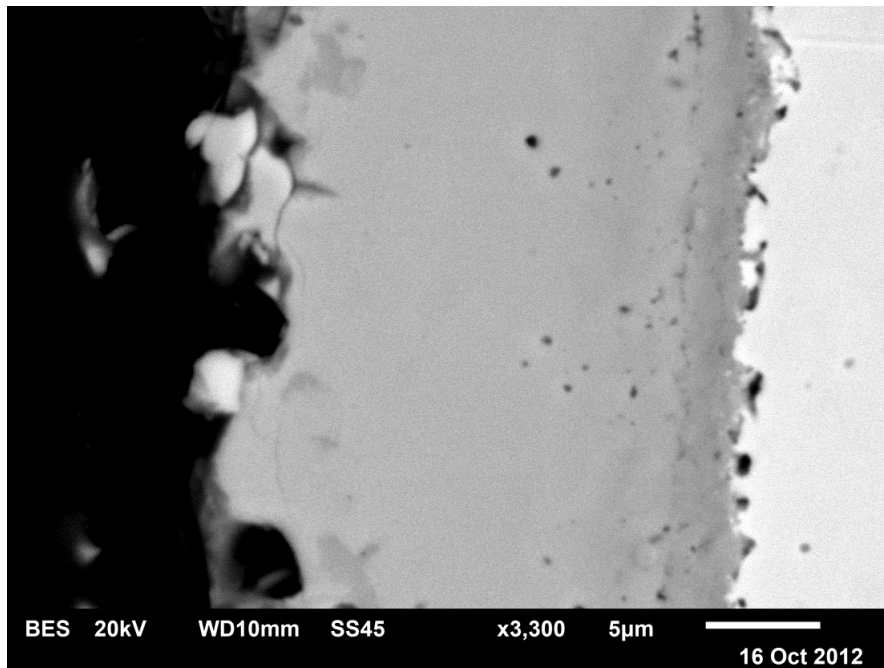


Figure 6-11: $\text{Ni}_{0.1}\text{Cu}_{1.1}\text{Mn}_{1.8}\text{O}_4$ spinel coating oxidized for 120 hours on 430 SS (ID 121-2).

Figure 6-12 shows the spinel after 24 hours of oxidation. Even after this time, the spinel was not fully formed, and a layer at the free-interface remained copper free. Directly under this region was a manganese rich oxide with impurities of iron. The remaining coating, except for the chromia scale, was a mix of iron, nickel and manganese oxides.

The low magnification image shows an exceptionally strong adhesion, likely due to the invasive diffusion of iron throughout the coating. Additionally, the free interface of the coating was highly damaged and porous. This was likely due to the high concentration of copper oxide.

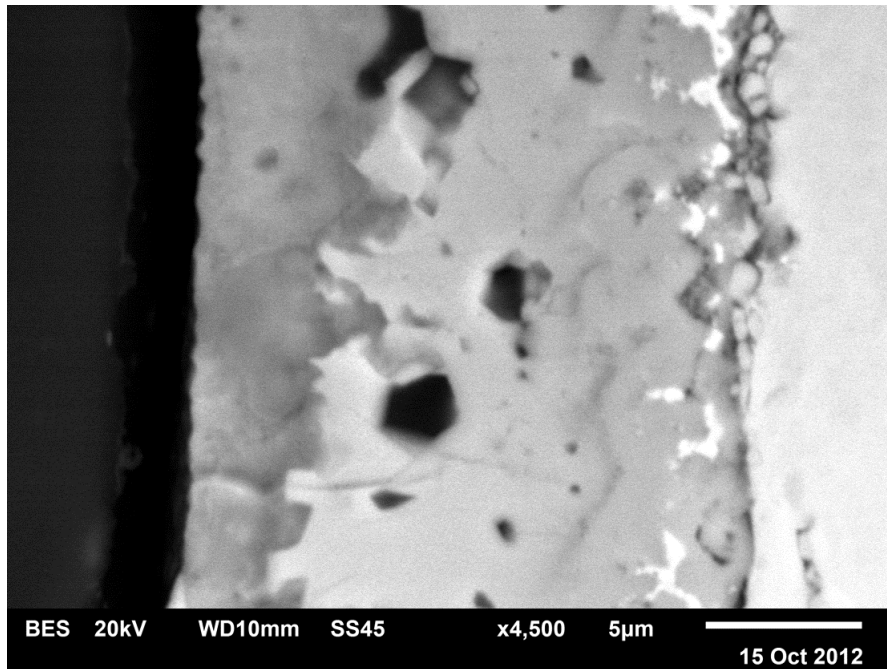


Figure 6-12: $\text{Ni}_{0.1}\text{Cu}_{1.1}\text{Mn}_{1.8}\text{O}_4$ spinel coating oxidized for 24 hours on Cr-5Fe (ID 124-2).

This is due to trapped copper behind the chromia scale. This manganese oxide layer was also present in the wide images, albeit sporadically. Other than this minor defect, which disappeared after longer oxidation times, the coating was acceptable. Unfortunately, the nitridation issue of chromium substrates remain.

Once the sample was oxidized for 120 hours, the spinel structure was fully equilibrated. In the wide-image, the coating was homogeneous, but some coating damage was present due to nitridation. Although the spinel formed the expected phase with few chromium

impurities, Figure 6-13 shows the formation of chromium-rich spinel, highlighted by the box. This phase was not often seen in this coating, but the thinned chromia scale could be responsible for the anomaly.

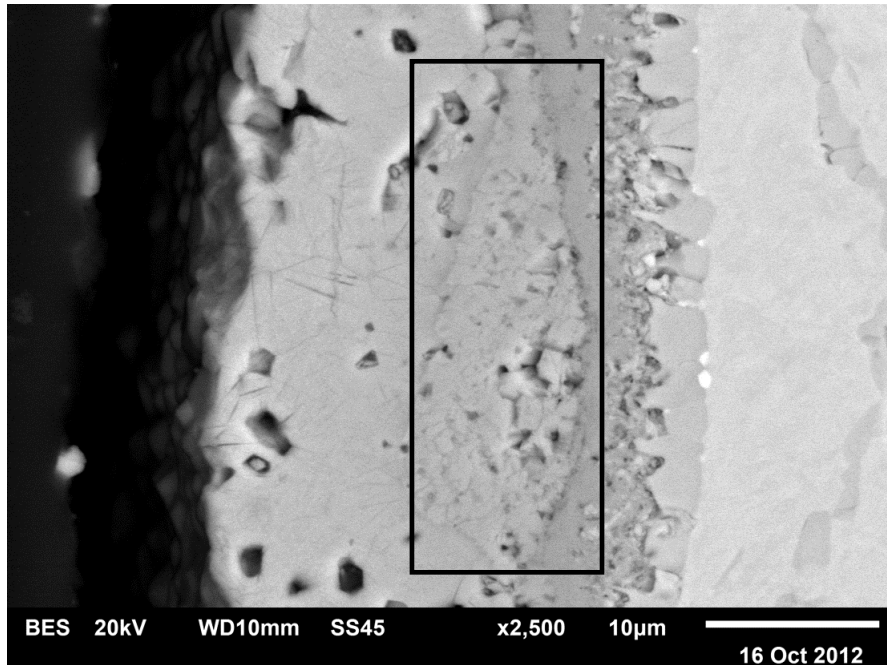


Figure 6-13: $\text{Ni}_{0.1}\text{Cu}_{1.1}\text{Mn}_{1.8}\text{O}_4$ spinel coating oxidized for 120 hours on Cr-5Fe (ID 118-2). Boxed highlights a chromium-rich spinel formed. This is a rare occurrence.

Semi-Stable Metallic Deposits

The extensive network of metallic deposits situated behind the chromia scale was very common for coatings applied to chromium substrates. In some cases, this could be seen in coatings for stainless steel samples. Although the metallic material, usually cobalt, copper or nickel, was plated on top of chromium containing material, a chromia scale formed around it before the deposit started to oxidize. Once covered with chromia, this deposit no longer reacted, due to the ability of chromia to block further oxygen transport. Chromia was much more stable than the oxides of cobalt, nickel, or copper. It is

important to note that no substantial amount of manganese was found in the metallic phase. Generally, no manganese of any form was found between the chromia and substrate, except in the case of the stainless steel. This is because the steel contained up to one weight percent of manganese. A possible mechanism for oxidation is proposed below.

During heat treatment, when most material was metallic, diffusion of oxygen and metals starts. At the same time, oxidation occurs. The oxygen affinity is the strongest for manganese, followed by chromium. Figure 6-14 shows the possible system state when both diffusion and oxidation has started. Manganese has oxidized, or as in the process of oxidation, while cobalt diffuses into that layer. Chromium has started to diffuse through cobalt. It is assumed that there was little diffusion of manganese towards the substrate, since there seems to be little manganese diffused beyond the chromia scale. Additionally, there is little diffusion of cobalt into the substrate, since cobalt is never detected beyond the cobalt-substrate interface.

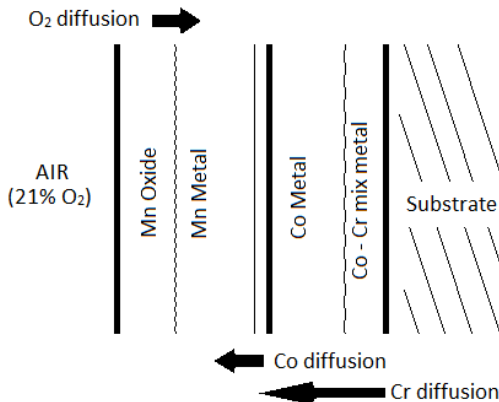


Figure 6-14: Start of Diffusion and Oxidation Processes.

Once the oxidation of manganese is complete, and the diffused manganese-cobalt layers have formed, the oxygen front within the coating encounters the chromium-cobalt mix metal layer. The chromium oxidizes preferentially over cobalt. This forms a chromia scale, which prevents (or slows) further diffusion of oxygen towards the substrate, as illustrated in Figure 6-15. However, the metal atoms could still travel the chromia scale, albeit at a slower rate. As chromium continues to penetrate through the scale, it becomes oxidized at the spinel-chromia interface. This increased the thickness of the chromia layer. Cobalt also continues to diffuse through the chromia layer, and enters the spinel structure. However, since there is a loss of material on one side of the chromia scale, defects start to form, as seen in Figure 6-16.

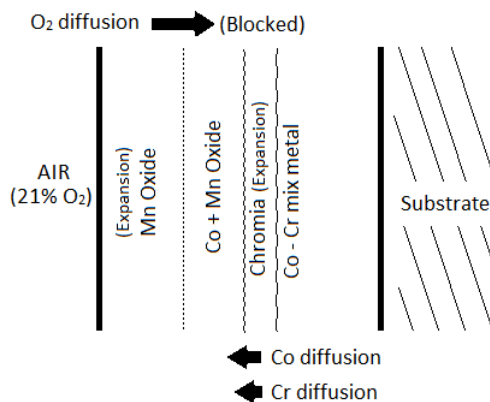


Figure 6-15: Intermediate step in diffusion and oxidation.

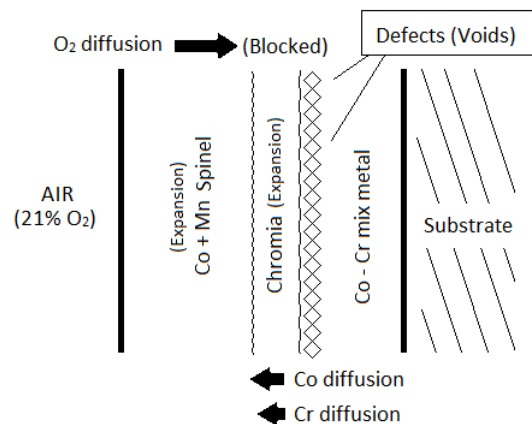


Figure 6-16: Steady State of diffusion and oxidation process.

This proposed mechanism is used to explain the occurrence of a metallic deposit at high temperatures, while in the presence of oxygen. It neglects to take into account the movement of nitrogen, and its effects on the structure. It also relies heavily on solid solution of metals, which is observed. Activity of both chromium and cobalt in solid

solutions would affect preferential oxidation. The formation of intermetallic compounds is ignored, as are the effects of thermal expansion and lattice change during oxidation. Finally, this needs validation of interdiffusion rates of cobalt, chromium, and manganese in their metallic and oxidized states.

Coating Damage and Defects

The coatings were not perfect. There were many defects that caused damage and delamination. At certain times, the substrate itself would introduce the impurities and defective material. In Figure 6-17, the surface of the substrate had a grain of aluminium, or alumina, embedded prior to coating. The source of this impurity could be a feed metal impurity. This would allow for aluminium to enter the coating system, with unknown consequences.

Improper cleaning of the substrate was another cause of damage to the coating. A silica grain, absorbed on the surface of the substrate was coated over, creating a region without adhesion, in Figure 6-18. Not only was the grain a source of additional impurities, the coating could fail at this point, or at the very least, cause issues with conductivity.

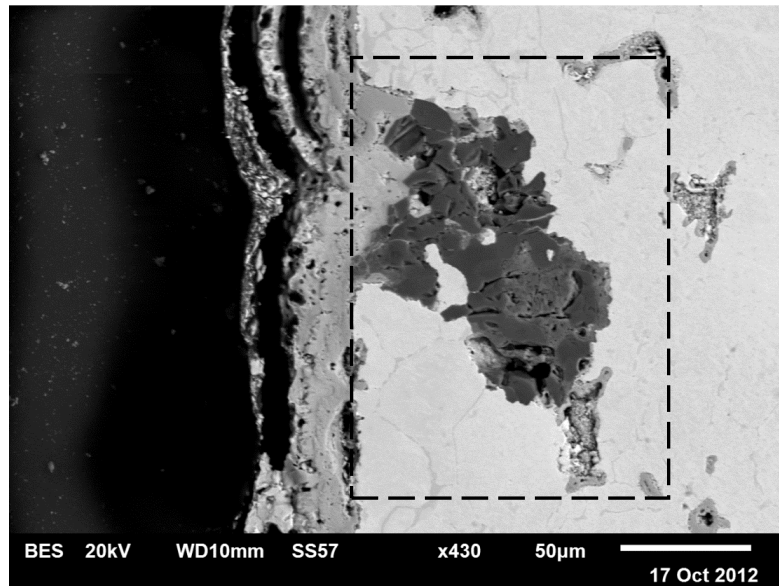


Figure 6-17: Inclusion of aluminium (or alumina) on Cr-5Fe substrate surface.

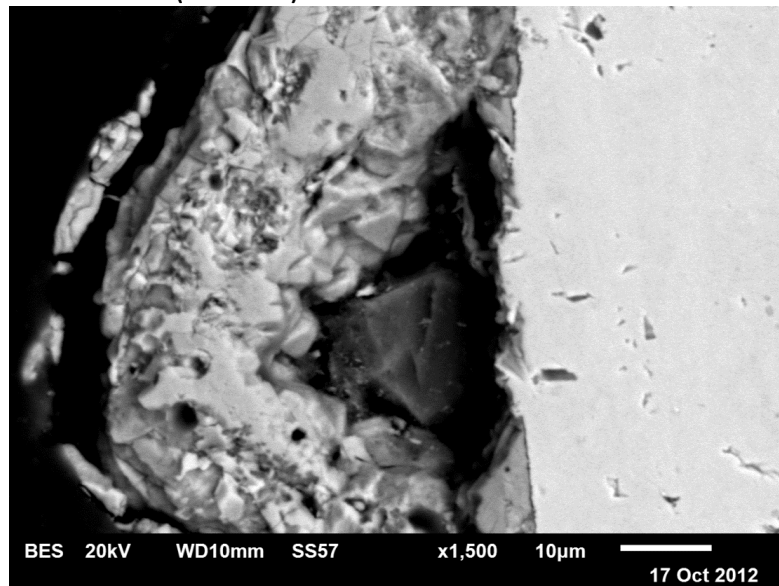


Figure 6-18: Silica grain preventing adhesion of coating.

Unfortunately, coating damage did not only occur due to improper preparation. Even with the most careful preparation, coatings would sometimes fail. The failure of coatings should be investigated further. One of the most common forms of coating damage was a bubbling effect in the upper layers of the coating, as in Figure 6-19 and Figure 6-20.

These could occur for multiple reasons. One possibility was that the uppermost layer, the manganese, was stressed and bulged during heat treatment. Another possibility was that the coating contained trapped liquids, or dissolved hydrogen. If excessive amounts of trapped fluids are forced out violently, this could possibly cause bubbling, which would eventually crack.

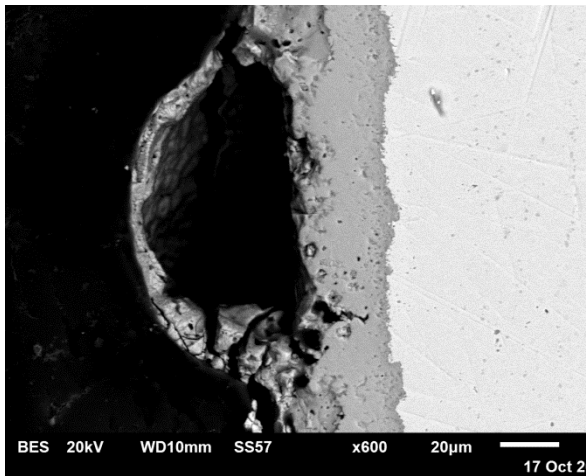


Figure 6-19: Large bubbling effect found in a Cu-Mn coating on 430 SS.

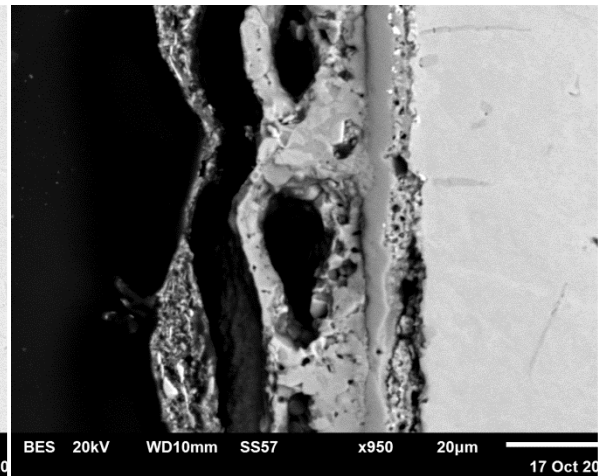


Figure 6-20: Successive small bubbling in Co-Mn coating on Cr-5Fe.

Originally, it was thought that this bubbling occurred only in copper-manganese spinels. However, cobalt spinels would at times exhibit this phenomenon. The final defect common in coatings was delamination. It was likely that coatings delaminate only during the cutting and polishing steps of the analysis process. Oxidized coatings generally do not spall unless excessive force was applied. However, the failure of the coating at localized areas could be cause for concern.

The spinel structure would fail to adhere to the chromia scale, as in Figure 6-21. This could be due to an improperly electropolished surface. If chromium oxide was on the surface prior to deposition of the coating, it is possible that no metal to metal bonding was established. The coating would fail once the heat treatment would begin. The failure at the chromia-substrate is generally only found in chromium substrates. This failure, seen in Figure 6-22, was likely related to the nitride formation.

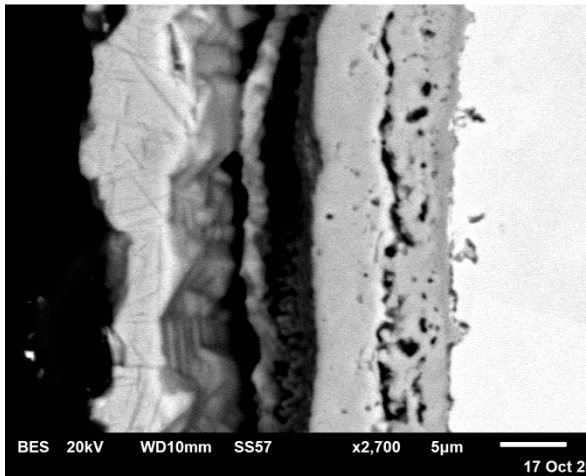


Figure 6-21: Coating failure at spinel-chromia interface.

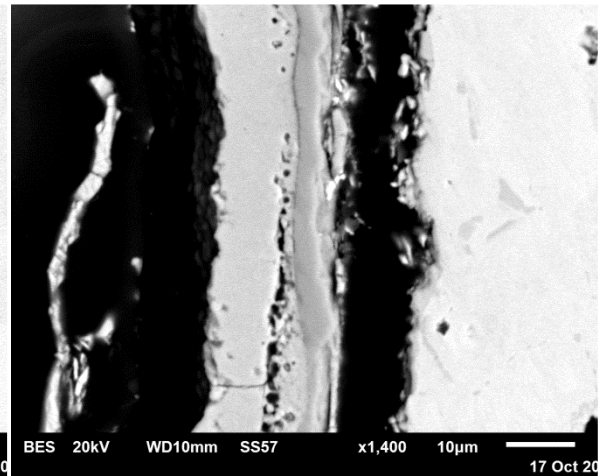


Figure 6-22: Coating failure at chromia-substrate interface.

Coating at Edges

Although not thoroughly reported in this thesis, edges have poor coating qualities. Figure 6-23 shows the common coating results when edge effects are present on the substrate surface. Nitridation and chromium scale growth exceeds the rest of the sample. In this case, the copper metal was poorly oxidized, and almost no manganese was present. It is obviously an important design factor when plating industrial sized plates, as this product was essentially the same as an uncoated plate.

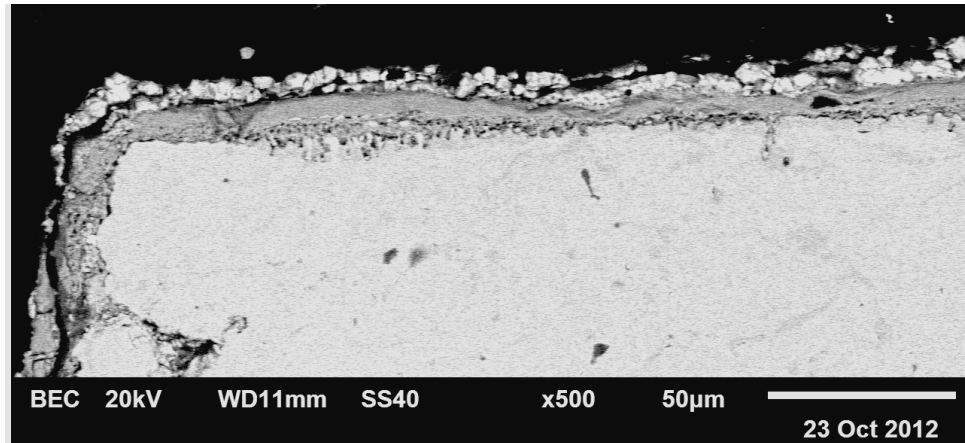


Figure 6-23: Common oxidation product at sample edge.

7. Summary and Conclusions

In this work, the production of spinel structured coatings was investigated. Two types of substrates, 430 stainless steel and a 95% chromium-5% iron alloy, were used to compare the quality of coatings. Spinels identified as candidates for interconnect coatings, due to their electrical, physical, and chemical properties, were tested. These spinels were from the cobalt-manganese and copper-manganese systems, which allowed for the deposition of their metallic components to be deposited by electrochemical reduction from aqueous solution.

Successfully electroplated samples were oxidized at 800°C for a period of time between 24 and 120 hours. While coatings of the copper-manganese system quickly oxidized within 24 hours, the cobalt-based coatings were not yet fully reacted after 120 hours. This was due to deposits of metallic solutions of cobalt and chromium, protected from oxidation by a thick chromia (Cr_2O_3) scale. However, these deposits showed size and quantity reduction between the 24 and 120 hour oxidation times.

The EDS analysis of coatings showed that cobalt-based coatings were generally better at suppressing the diffusion of iron and chromium. However, when placed on stainless steel substrates, iron diffusion was aggressive, displacing cobalt in the structure. Of copper-based coatings, only those with slight additions of nickel seemed beneficial. A proper balance between copper and manganese was necessary to produce adequate coatings.

The deposition processes used in both cobalt- and copper-based spinels were easily scaled to industrial sized interconnects. The control of plating parameters in larger baths

was more difficult, but just as important. Although the processes used in the electrodeposition of these coatings are robust, special care must be taken to keep them from straying.

Future Work

The successful oxidation of metallic layers must be improved before spinels can replace other coatings. Several key aspects of the oxidation process should be understood, and controlled, for this to happen.

First, the nitridation of the chromium plates is the root of many problems for this type of substrate. This nitride formation occurs during oxidation, and a successful method of negating this phenomenon would provide increased adhesion.

Second, the prevention of metallic cobalt deposits will allow for the spinel to form at intended compositions. A better understanding of the diffusion and oxidation processes is needed for this to be achieved.

Lastly, low levels of iron and chromium impurities were seen in the spinel coating after only 120 hours of oxidation time. For fuel cells to have a lifetime of 40,000 hours or more, further suppression of these impurities will be needed. An investigation into the porosity of the spinel coating, and the possibility of reducing coating “bubbling” is suggested.

8. Bibliography

- Baliga, S., & Jain, A. L. (1990). Electrical Conduction and Ordering in $\text{Cu}_x\text{Ni}_{1-x}\text{Mn}_2\text{O}_4$ Spinels. *Materials Letters*, 9, 180-184.
- Bard, A. J., & Faulkner, L. R. (2001). *Electrochemical Methods; Fundamentals and Applications* (2nd ed.). USA: John Wiley & Sons, Inc.
- Bateni, M. R., Wei, P., Deng, X., & Petric, A. (2007). Spinel Coatings for UNS 430 stainless steel interconnects. *Surface & Coatings Technology*, 201, 4677-4694.
- Bordeneuve, H., Tenailleau, C., Guillemet-Fritsch, S., Smith, R., Suard, E., & Rousset, A. (2010). Structural variations and cation distributions in $\text{Mn}_{3-x}\text{Co}_x\text{O}_4$ ($0 < x < 3$) dense ceramics using neutron diffraction data. *Solid State Sciences*, 379-386.
- Ebbinghaus, B. B. (1993). Thermodynamics of Gas Phase Chromium Species: The Chromium Oxides, the Chromium Oxyhydroxides, and Volatility Calculations in Waste Incineration Processes. *Combustion and Flame*, 119-137.
- Elbadraoui, E., Baudour, J. L., Bouree, F., Gillot, B., Fritsch, S., & Rousset, A. (1997). Cation distribution and mechanism of electrical conduction in nickel-copper manganite spinels. *Solid State Ionics*, 219-225.
- Gabe, D. R. (1997). The role of hydrogen in metal electrodeposition processes. *Journal of Applied Electrochemistry*, 27, 908-915.
- Gong, J., & Zangari, G. (2002). Electrodeposition and Characterization of Manganese Coatings. *Journal of the Electrochemical Society*, 149 (4), C209-C217.
- Gong, J., & Zangari, G. (2004). Electrodeposition and Characterization of Sacrificial Copper-Manganese Alloy Coatings. *Journal of the Electrochemical Society*, 151 (5), C297-C306.
- Gong, J., & Zangari, G. (2004). Increased Metallic Character of Electrodeposited Mn Coatings Using Metal Ion Additives. *Electrochemical and Solid-State Letters*, C91-C94.
- Hilpert, K., Das, D., Miller, M., Peck, D., & Weib, R. (1996). Chromium Vapor Species over Solid Oxide Fuel Cell Interconnect Materials and Their Potential for Degradation Processes. *Journal of the Electrochemical Society*, 143 (11), 3642-3647.
- Huang, K., & Goodenough, J. B. (2009). *Solid oxide fuel cell technology: Principles, performance and operations*. New Dehli: Woodhead Publishing in Energy.
- Jeffrey, M. I., Choo, W. L., & Breuer, P. L. (2000). The Effects of Additives and Impurities on the Cobalt Electrowinning Process. *Minerals Engineering*, 13, 1231-1241.

Kongstein, O. E., Haarberg, G. M., & Thonstad, J. (2007). Current efficiency and kinetics of cobalt electrodeposition in acid chloride solutions. Part I: The influence of current density, pH, and temperature. *Journal of Applied Electrochemistry*, *37*, 669-674.

Kshirsagar, S. T. (1969). Electrical and Crystallographic Studies of the System $\text{Cu}_x\text{Ni}_{(1-x)}\text{Mn}_2\text{O}_4$. *Journal of the Physical Society of Japan*, *27*, 1164-1170.

Legros, R., Metz, R., & Rousset, A. (1995). The Preparation, Characterization and Electrical Properties of Electroceramics made of Copper-Cobalt Manganite Spinel: $\text{Mn}_{(2.6-x)}\text{Co}_{(0.4)}\text{Cu}_x\text{O}_4$, $0 < x < 1$. *Journal of the European Ceramic Society*, *15*, 463-468.

Lewis, J. E., Scaife, P. H., & Swinkels, D. A. (1976). Electrolytic manganese metal from chloride electrolytes. II. Effect of additives. *Journal of Applied Electrochemistry*, *6*, 453-462.

Lowenheim, F. A. (1978). *Electroplating*. USA: McGraw-Hill.

Lu, J., Yang, Q.-H., & Zhang, Z. (2010). Effects of additives on nickel electrowinning from sulfate system. *Trans. Nonferrous Met. Soc. China*, *20*, s97-s101.

Newbery, E. (1916). Overvoltage Tables. Part I. Cathodic Over-voltages. *Journal of the Chemical Society*, 1051-1066.

Nikolic, N. D., Popov, K. I., Pavlovic, L. J., & Pavlovic, M. G. (2006). The effect of hydrogen codeposition on the morphology of copper electrodeposits. I. The concept of effective overpotential. *Journal of Electroanalytical Chemistry*, *588*, 88-98.

Ogata, Y., Yamakawa, K., & Yoshizawa, S. (1983). Concentration dependence of the morphology of electrodeposits and criterion for the morphological change of copper electrodeposits. *Journal of Applied Electrochemistry*, *13*, 611-617.

Pattarkine, G. V., Dasgupta, N., & Virkar, A. V. (2008). Oxygen Transport Resistant and Electrically Conductive Perovskite Coatings for Solid Oxide Fuel Cell Interconnects. *Journal of the Electrochemical Society*, *155*, B1036-B1046.

Petric, A., & Ling, H. (2007). Electrical Conductivity and Thermal Expansion of Spinel at Elevated Temperatures. *J. Am. Ceram. Soc.*, *90* (5), 1515-1520.

Pradhan, N., Singh, P., Tripathy, B. C., & Das, S. C. (2001). Electrowinning of Cobalt from Acidic Sulphate Solutions-Effects of Chloride Ion. *Minerals Engineering*, *14* (7), 775-783.

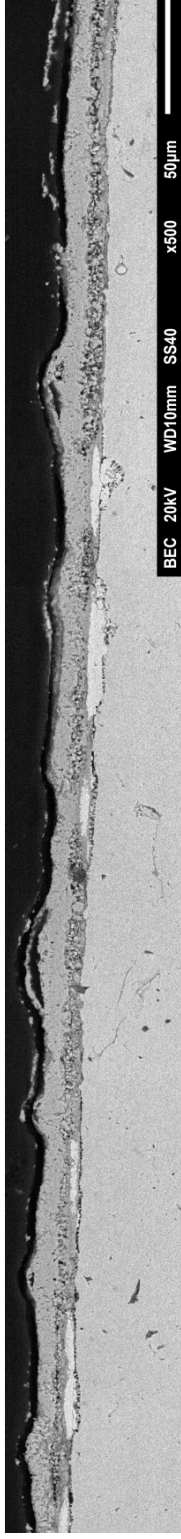
Press, R. J., Santhanam, K., Miri, M. J., Bailey, A. V., & Takacs, G. A. (2009). *Introduction to Hydrogen Technology*. New Jersey: John Wiley & Sons, Inc.

- Radhakrishnamurthy, P., & Reddy, A. K. (1977). Mechanism of action of selenious acid in the electrodeposition of manganese. *Journal of Applied Electrochemistry*, 7, 113-117.
- Santos, J. S., Matos, R., Trivinho-Strixino, F., & Pereira, E. C. (2007). Effect of temperature on Co electrodeposition in the presence of boric acid. *Electrochimica Acta*, 53, 644-649.
- Schlesinger, M., & Paunovic, M. (Eds.). (2000). *Modern Electroplating* (4th ed.). USE: John Wiley & Sons, Inc.
- Shaigan, N., Qu, W., Ivey, D. G., & Chen, W. (2010). A review of recent progress in coatings, surface modifications and alloy developments for solid oxide fuel cell ferritic stainless steel interconnects. *Journal of Power Sources*, 195, 1529-1542.
- Sharma, I. G., Alex, P., Bidaye, A. C., & Suri, A. K. (2005). Electrowinning of cobalt sulphate solutions. *Hydrometallurgy*, 80, 132-138.
- Stanislawski, M., Froitzheim, J., Niewolak, L., Quadackers, W. J., Hilpert, K., Markus, T., et al. (2007). Reduction of chromium vaporization from SOFC interconnectors by highly effective coatings. *Journal of Power Sources*, 164, 578-589.
- Suzuki, M. (1980). A.C. Hopping Conduction in Mn-Co-Ni-Cu Complex Oxide Semiconductors with Spinel Structure. *J. Phys. Chem. Solids*, 41, 1253-1260.
- Sylla, D., Savall, C., Gadouleau, M., Rebere, C., Creus, J., & Refait, P. (2005). Electrodeposition of Zn-Mn alloys on steel using an alkaline pyrophosphate-based electrolytic bath. *Surface & Coating Technology*, 200, 2137-2145.
- Trebbels, R., Markus, T., & Singheiser, L. (2009). Reduction of Chromium Evaporation with Manganese-Based Coatings. *ECS Transactions*, 25, 1417-1422.
- Tsuru, Y., Nomura, M., & Foulkes, F. R. (2002). Effects of boric acid on hydrogen evolution and internal stress in films deposited from a nickel sulfamate bath. *Journal of Applied Electrochemistry*, 32, 629-634.
- Vicenzo, A., & Cavallotti, P. L. (2002). Copper electrodeposition from a pH 3 sulfate electrolyte. *Journal of Applied Electrochemistry*, 32, 743-753.
- Walker, R., & Ward, A. (1970). Stress in Copper Electrodeposits from the Sulfate Bath. *Electrochimica Acta*, 15, 673-679.
- Wei, P., Deng, X., Batani, M. R., & Petric, A. (2007). Oxidation and Electrical Conductivity Behavior of Spinel Coatings for Metallic Interconnects of Solid Oxide Fuel Cells. *Corrosion Science*, 63 (6), 529-536.

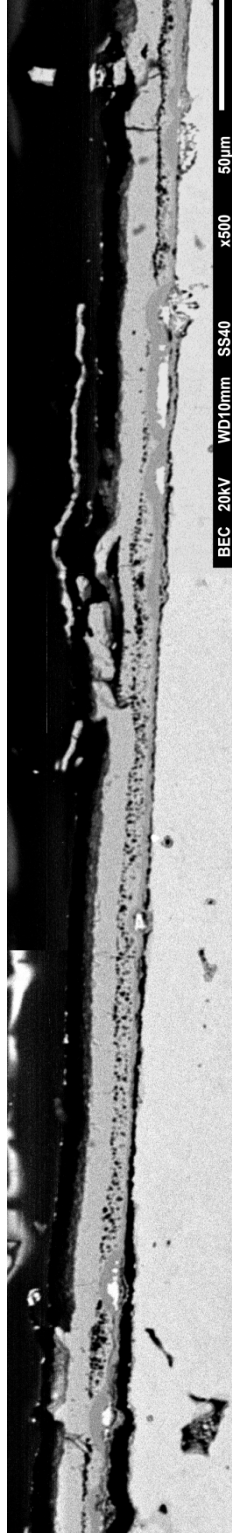
Wei, P., Hileman Jr, O. E., Bateni, M. R., Deng, X., & Petric, A. (2007). manganese deposition without additives. *Surface & Coatings Technology*, 201, 7739-7745.

Xu, Y., Wen, Z., Wang, S., & Wen, T. (2011). Cu doped Mn-Co spinel protective coating on ferritic stainless steels for SOFC interconnect applications. *Solid State Ionics*, 192, 561-564.

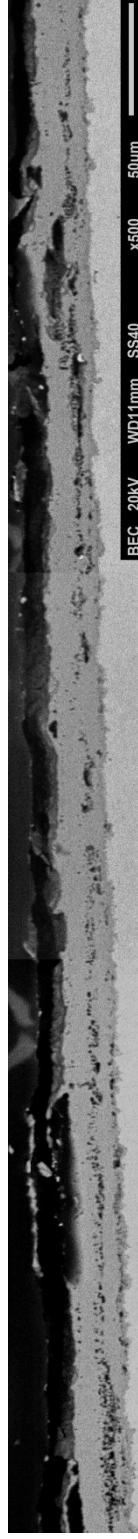
Appendix A: Low Magnification Cross-sections Images



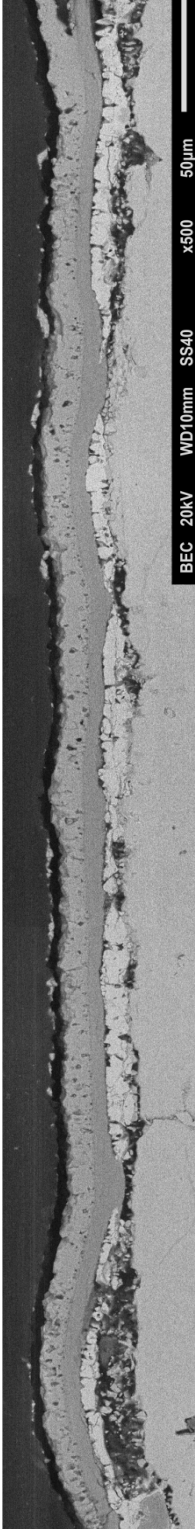
Cross-Section of MnCo₂O₄ spinel oxidized for 24 hours on Cr-5Fe (ID 124-3).



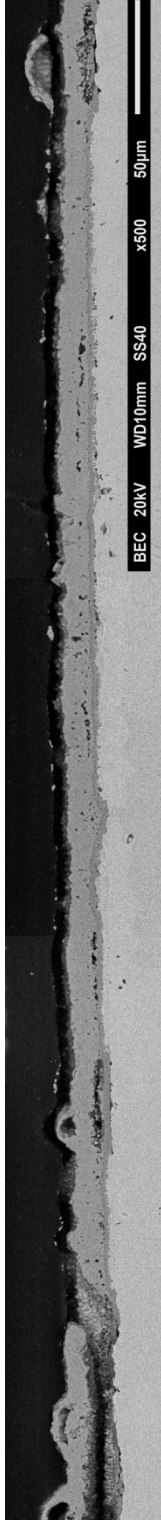
Cross-Section of MnCo₂O₄ spinel oxidized for 120 hours on Cr-5Fe (ID 114-1a).



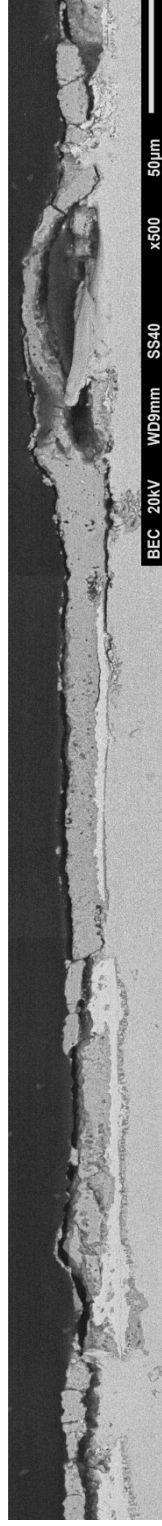
Cross-Section of MnCo₂O₄ spinel oxidized for 120 hours on 430 SS (ID 114-1b).



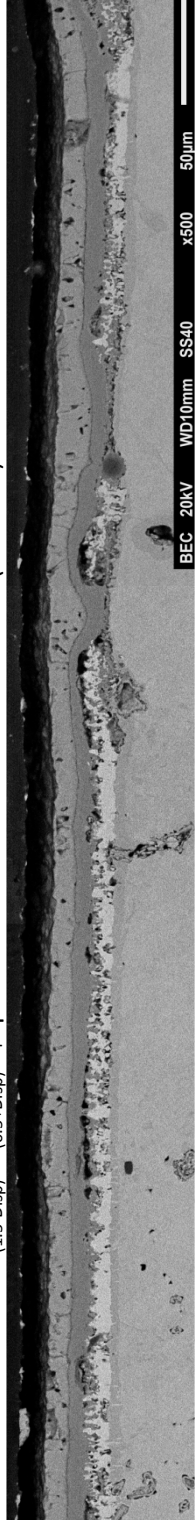
Cross-Section of $\text{MnCo}_{(2-\text{disp})}\text{Cu}_{(0.5+\text{disp})}\text{O}_4$ spinel oxidized for 120 hours on Cr-5Fe (ID 114-2a).



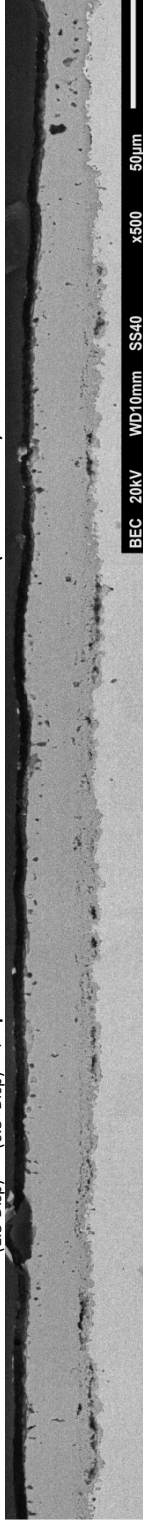
Cross-Section of $\text{MnCo}_{(2-\text{disp})}\text{Cu}_{(0.5+\text{disp})}\text{O}_4$ spinel oxidized for 120 hours on 430 SS (ID 114-2b).



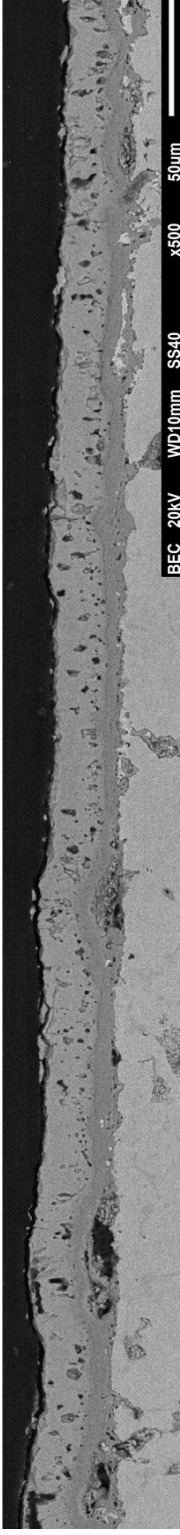
Cross-Section of $\text{MnCo}_{(1.5-\text{disp})}\text{Cu}_{(0.5+\text{disp})}\text{O}_4$ spinel oxidized for 24 hours on Cr-5Fe (ID 124-4).



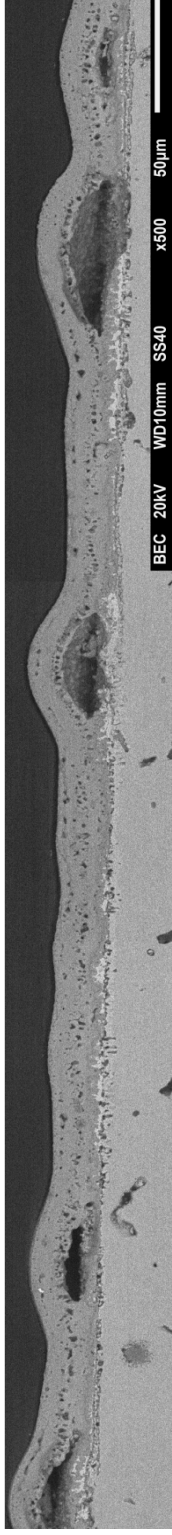
Cross-Section of $\text{MnCo}_{(1.5-\text{disp})}\text{Cu}_{(0.5+\text{disp})}\text{O}_4$ spinel oxidized for 120 hours on Cr-5Fe (ID 114-3a).



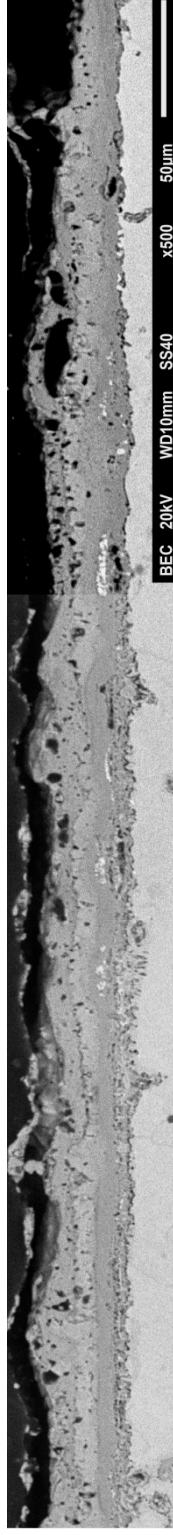
Cross-Section of $\text{MnCo}_{(1.5-\text{disp})}\text{Cu}_{(0.5+\text{disp})}\text{O}_4$ spinel oxidized for 120 hours on 430 SS (ID 114-2b).



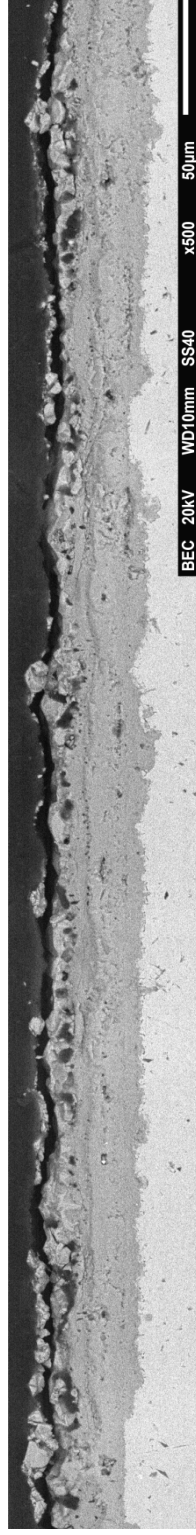
Cross-Section of $\text{Cu}_{0.7}\text{Ni}_{0.5}\text{Mn}_{1.8}\text{O}_4$ spinel oxidized for 120 hours on Cr-5Fe (ID 117-1).



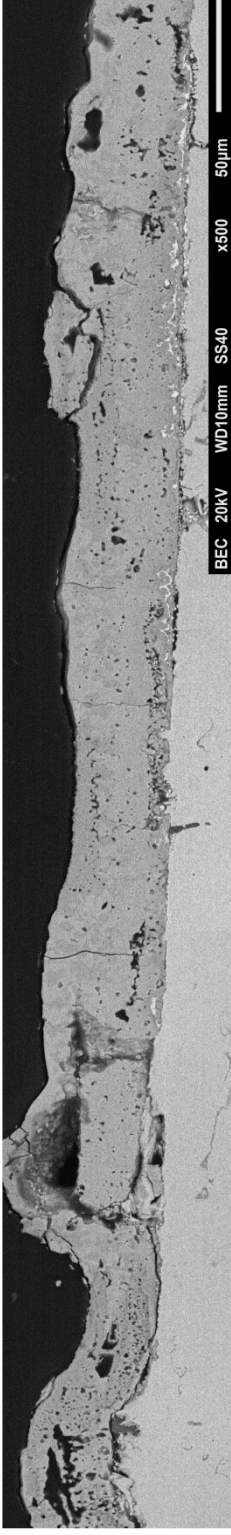
Cross-Section of $\text{Cu}_{0.7}\text{Ni}_{0.1}\text{Mn}_{2.2}\text{O}_4$ spinel oxidized for 24 hours on Cr-5Fe (ID 124-1)



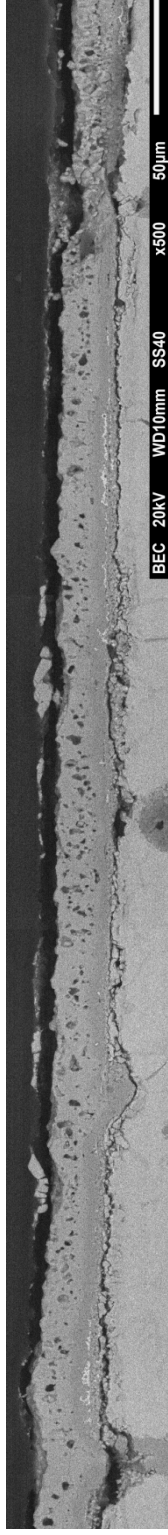
Cross-Section of $\text{Cu}_{0.7}\text{Ni}_{0.1}\text{Mn}_{2.2}\text{O}_4$ spinel oxidized for 120 hours on Cr-5Fe (ID 117-2)



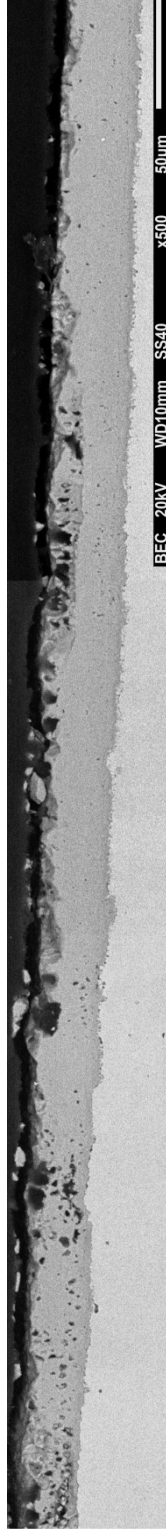
Cross-Section of $\text{Cu}_{0.7}\text{Ni}_{0.1}\text{Mn}_{2.2}\text{O}_4$ spinel oxidized for 120 hours on 430 SS (ID 121-1)



Cross-Section of $\text{Cu}_{1.1}\text{Ni}_{0.1}\text{Mn}_{1.8}\text{O}_4$ spinel oxidized for 24 hours on Cr-5Fe (ID 124-2)



Cross-Section of $\text{Cu}_{1.1}\text{Ni}_{0.1}\text{Mn}_{1.8}\text{O}_4$ spinel oxidized for 120 hours on Cr-5Fe (ID 118-2)



Cross-Section of $\text{Cu}_{1.1}\text{Ni}_{0.1}\text{Mn}_{1.8}\text{O}_4$ spinel oxidized for 120 hours on 430 SS (ID 121-2)

Appendix B: Material Analysis

Index of reagents used in thesis work.

<u>Alfa Aesar</u>					
<u>Chemical</u>	<u>Assay</u>	<u>MW</u>	<u>Details</u>	<u>Stock #</u>	<u>Lot #</u>
MnSO ₄ ·H ₂ O	Yes	169.02	98.0% - 101.0%	33341	A15W006
CuSO ₄ ·5H ₂ O	Yes	249.68	99%	A11262	10151600
Na ₂ SO ₄ ·10H ₂ O	No	322.19	99%	A15702	10164019
(NH ₄) ₂ SO ₄	Yes	132.14	98+%	A11682	10157943
CoCl ₂ ·6H ₂ O	Yes	237.93	98-102%	36554	G11Q09
<u>Caledon Labs</u>					
<u>Chemical</u>	<u>Assay</u>	<u>MW</u>	<u>Details</u>	<u>Stock #</u>	<u>Lot #</u>
H ₃ BO ₃	Yes	61.84	~99%	2260-1	67157
(NH ₄)OH	No	35.05	28.0-30.0%	1525-1	460108
NH ₄ Cl	No	53.49	~99%	1320-1	69469
NH ₂ OH·HCl	No	69.49	99%	4091-5	60690
<u>EMD</u>					
<u>Chemical</u>	<u>Assay</u>	<u>MW</u>	<u>Details</u>	<u>Stock #</u>	<u>Lot #</u>
NiSO ₄ ·6H ₂ O	Yes	262.85	98.0-102.0%	NX0350-1	47123721
<u>Sigma-Aldrich</u>					
<u>Chemical</u>	<u>Assay</u>	<u>MW</u>	<u>Details</u>	<u>Stock #</u>	<u>Lot #</u>
SeO ₂	Yes	110.96	≥99.9%	200107-25G	03305CC

Cobalt (II) chloride hexahydrate, ACS, 98.0-102.0%

Stock Number: 36554
Lot Number: G11Q09

Product No.: A11682

Product: Ammonium sulfate, 98+%

Lot No.: 10157943

Analysis

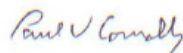
Test	Limits	Results
Assay	98.0 – 102.0 %	99.6 %
Insoluble	0.01 % max	< 0.01 %
Nitrate	0.01 % max	< 0.01 %
Sulfate	0.01 % max	< 0.01 %
Copper	0.002 % max	< 0.002 %
Nickel	0.1 % max	< 0.003 %
Zinc	0.03 % max	< 0.001 %
Iron	0.005 % max	< 0.001 %
Calcium	0.005 % max	< 0.001 %
Magnesium	0.005 % max	< 0.001 %
Potassium	0.01 % max	< 0.001 %
Sodium	0.05 % max	< 0.001 %

Traceable to NIST? Yes

Typical Analysis

Appearance	White, crystalline material
Assay	98 % min
Nitrogen	21 % min
Free H ₂ SO ₄	< 0.01 %
Water	0.07 %
Sulfated ash	0.05 %
Cyanide	< 1 ppm
Phenols	< 2 ppm
Al	< 1
As	< 0.1
Cr	< 2
F	< 10
Pb	< 0.5
Hg	< 0.5
Se	< 0.1
Zn	1
Sb	< 0.02
Cd	< 0.1
Cu	< 0.5
Fe	13
Mn	< 1
Ni	< 2
Ag	1

Certified by:



Quality Control

Values given in ppm unless otherwise noted

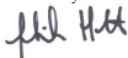
Manganese(II) sulfate monohydrate, ACS, 98.0-101.0%

Stock Number: 33341
Lot Number: A15W006

Analysis

Test	Limits	Results
Assay	98.0 - 101.0 %	99.9 %
Insoluble matter	0.01 % max	0.006 %
Substances reducing KMnO ₄	To pass test	Passes
Heavy metals (as Pb)	0.002 % max	0.001 %
Iron	0.002 % max	0.001 %
Zinc	0.005 % max	0.0001 %
Calcium	0.005 % max	0.001 %
Nickel	0.02 % max	0.008 %
Chloride	0.005 % max	0.004 %
Magnesium	0.005 % max	0.003 %
Potassium	0.01 % max	0.0001 %
Sodium	0.05 % max	0.0002 %
Loss on ignition	10.0 - 12.0 %	10.8 %
pH (5 % solution at 25°C)		3.2
Identification		Passes
Substances not precipitated by ammonium sulfide		0.02 %
Organic volatile impurities		Passes

Certified by:



Quality Control

Name: Nickel Sulfate Hexahydrate
GR ACS
Meets ACS Specifications

Formula: $\text{NiSO}_4 \cdot 6\text{H}_2\text{O}$

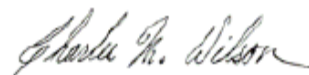
Item Number: NX0350/1, NX0350/20, NX0350/4, NX0350/5,
NX0350/6, NX0350/7, NX0350/901

Formula Wt: 262.85

Lot Number: 47123721

Data Order No: 000409128

CHARACTERISTIC	REQUIREMENT		RESULTS	UNITS
	Min.	Max.		
Assay (complexometric)	98.0	102.0	100.60	%
Insoluble matter		0.005	0.0040	%
Color			Blue-green	
Form			Crystals	
Chloride (Cl)		0.001	0.0008	%
Nitrogen compounds (as N)		0.002	0.0016	%
Calcium (Ca)		0.005	0.0030	%
Cobalt (Co)		0.002	0.0016	%
Copper (Cu)		0.005	0.0025	%
Iron (Fe)		0.001	0.0007	%
Magnesium (Mg)		0.005	0.0020	%
Manganese (Mn)		0.002	0.0015	%
Potassium (K)		0.01	0.0040	%
Sodium (Na)		0.05	0.0080	%



Charles M. Wilson,
Quality Assurance Manager

Release Date: 5/9/2007

EMD Chemicals Inc.
(Formerly EM Science, A Division of EM Industries, Inc.)
An Affiliate of Merck KGaA, Darmstadt, Germany

Product Name AMMONIUM CHLORIDE

Item Number 1320-1-70

Chemical Formula NH₄Cl

Lot Number 69469

Formula Weight 53.49

Date Issued Wednesday, September 05, 2012

UN Number N/A

Gradename Reagent

CAS Number 12125-02-9

<i>Test Description</i>	<i>UoM</i>	<i>Limit</i>	<i>Result</i>
Meets ACS Specifications		-	-
Assay	%	Min. 99.5	100.4
pH of a 5 % solution at 25 °C	N/A	4.5 to 5.5	4.9
Maximum Allowable		-	-
Insoluble matter	%	0.005	< 0.005
Residue after ignition	%	0.01	< 0.01
Phosphate (PO ₄)	ppm	2	< 2
Sulphate (SO ₄)	%	0.002	< 0.002
Calcium (Ca)	%	0.001	< 0.001
Magnesium (Mg)	ppm	5	< 5
Heavy metals (as Pb)	ppm	5	< 5
Iron (Fe)	ppm	2	< 2

Product Name BORIC ACID

Item Number 2260-1-70

Chemical Formula H₃BO₃

Lot Number 67157

Formula Weight 61.83

Date Issued Thursday, September 06, 2012

UN Number N/A

Gradename Reagent

CAS Number 10043-35-3

<i>Test Description</i>	<i>UoM</i>	<i>Limit</i>	<i>Result</i>
Meets ACS Specifications		-	-
Assay	%	Min. 99.5	99.8
Maximum Allowable		-	-
Insoluble in methanol	%	0.005	< 0.005
Non-volatile with methanol	%	0.05	< 0.05
Chloride (Cl)	%	0.001	< 0.001
Phosphate (PO ₄)	%	0.001	< 0.001
Sulphate (SO ₄)	%	0.01	< 0.01
Calcium (Ca)	%	0.005	< 0.005
Heavy metals (as Pb)	%	0.001	< 0.001
Iron (Fe)	%	0.001	< 0.001

Appendix C: Pourbaix Diagram for various aqueous metal ions.

